



Parameterizing tidal-water intrusions in long-term Antarctic ice-sheet projections

Antonio Juarez-Martinez^{1,2}, Alexander Robinson³, Jan Swierczek-Jereczek^{1,2}, Javier Blasco³, Jorge Alvarez-Solas², and Marisa Montoya^{1,2}

¹Department of Earth Physics and Astrophysics, Complutense University of Madrid, Madrid, Spain

²Geosciences Institute CSIC-UCM, Madrid, Spain

³Alfred Wegener Institute, Helmholtz Centre for Polar and Marine Research, Potsdam, Germany

Correspondence: Antonio Juarez-Martinez (antjua01@ucm.es)

Abstract. The Antarctic Ice Sheet is expected to be the dominant contributor to sea-level rise in the coming centuries. However, this contribution is deeply uncertain due to the lack of understanding of some fundamental processes influencing ice-sheet dynamics. A key question is the extent to which submarine melting takes place at the transition between grounded and floating ice. Traditionally, in continental-scale ice-sheet modelling, this area has been treated as an abrupt transition or grounding line with suppressed or strongly limited submarine melting upstream. However, several lines of evidence challenge this view. In many places, changes in ocean tides lead to back and forth migrations of the grounding line over a broad grounding zone and can cause intrusion of warm ocean waters several kilometres upstream of the grounding line, allowing for submarine melting there. Here, we propose a simple parameterization to represent the effect of tidally-controlled migrations of the grounding line and tidal-water intrusion in submarine melting in continental-scale ice-sheet models. We calibrate the magnitude of the parameter controlling the extent of oceanic water intrusions against the observational evidence as inferred from differential interferometry synthetic aperture radar. We use a three-dimensional ice-sheet model to investigate the impact of this parameterization on Antarctic ice-sheet projections under a high-emission climate scenario extending to the year 3000. Our results show that increasing the extent of tidal intrusion, reinforced by dynamic feedbacks, leads to stronger and more widespread grounding-zone retreat under warming scenarios, and consequently ice-stream acceleration, ice-shelf thinning and debuttressing. This implies larger sea-level contributions compared to the usual treatment of melt at the grounding line and should be accounted for in future projections.

1 Introduction

The Antarctic Ice Sheet (AIS) contains an ice volume of approximately 58 meters of sea-level equivalent (SLE; Morlighem et al., 2020). Over the past two decades (2002–2022), an average of 127 ± 23 Gt yr⁻¹ of ice has been lost (Diener et al., 2021; Hanna et al., 2024). This loss is concentrated in the West Antarctic Ice Sheet (WAIS; Greene et al., 2022; Otosaka et al., 2023) and is largely due to enhanced submarine melting and thinning of ice shelves in this area (Shepherd et al., 2019), which has led to a reduction in the ice-shelf buttressing of the ice sheet, acceleration of the ice flow, and increasing ice discharge (Miles and Bingham, 2024).



The AIS will likely become the dominant contributor to sea-level rise in the next centuries (Seroussi et al., 2020, 2024). Model studies agree in pointing to ice-ocean interactions as the main driver of ice loss via enhanced sub-shelf melting and calving (Turney et al., 2020; Bett et al., 2024; Coulon et al., 2024; Juarez-Martinez et al., 2024; Coulon et al., 2025; Fricker et al., 2025). The incomplete understanding of these and other fundamental processes influencing ice-sheet dynamics, the spread in the representation of these processes, and the potential tipping behaviour of the AIS imply that the future contribution to sea-level rise is deeply uncertain (Fox-Kemper et al., 2021; Coulon et al., 2025). For high-emission scenarios, the sea-level contribution (SLC) by 2300 within the Ice Sheet Model Intercomparison Project (ISMIP6) ranges from -0.6 up to 4.4 m SLE (Seroussi et al., 2024). The upper-range values result from a collapse of the WAIS, where sectors such as the Amundsen Sea Embayment are highly prone to destabilization through enhanced submarine melting (Paolo et al., 2023; Alevropoulos-Borrill et al., 2024; Hill et al., 2024). Large areas of the WAIS are grounded on retrograde bedrock and therefore potentially subject to the marine ice-sheet instability (MISI; Weertman, 1974; Schoof, 2007), which underlies the high-range estimates of ISMIP6 (Seroussi et al., 2024): when the grounding line (GL), the location where ice loses contact with the bed, of a marine ice sheet retreats over a retrograde bedrock, the ice thickness at the GL increases. Because ice flux at the GL increases nonlinearly with ice thickness, this results in higher ice discharge, promoting further retreat of the GL, initiating a positive feedback loop that can lead to unstable and potentially rapid retreat of the ice sheet (Pattyn, 2018).

A critical issue in this context is the treatment of submarine melting at the GL. Traditionally, it has been considered to behave as a hydraulic barrier to seawater intrusion beneath grounded ice due to the large horizontal hydropotential gradient imposed by the increasing ice thickness upstream (Robel et al., 2022). Therefore, it has been conceived as a semi-fixed, abrupt transition from grounded to floating ice that migrates only over short distances (100–200 m) during the tidal cycle as it maintains hydrostatic equilibrium (Rignot et al., 2011), with suppressed or strongly limited submarine melting upstream, under grounded ice.

However, several lines of recent evidence challenge this view, suggesting that warm ocean waters can intrude several kilometres upstream of the GL (Chen et al., 2023; Rignot et al., 2024). On one hand, subglacial water is discharged to the ocean close to the GL. Where this cold but fresh water meets warm, salty ocean water, the denser warm and salty ocean water forces the lower density freshwater to rise, creating a salty wedge that can intrude horizontally upstream of the GL (MacGregor et al., 2011; Horgan et al., 2013; Milillo et al., 2019; Wilson et al., 2020; Robel et al., 2022). In addition, the GL migrates back and forth with changes in oceanic tides over much larger distances than those predicted by hydrostatic equilibrium. Tidally controlled migration of the GL by 2–18 km has been documented in several regions such as Pine Island Glacier (Milillo et al., 2017), Thwaites Glacier (Milillo et al., 2019), the Getz Ice Shelf (Mohajerani et al., 2021), the southern Ronne Ice Shelf (Freer et al., 2023), the Amery Ice Shelf (Zhu et al., 2025) and Berry Glacier (Chen et al., 2025). Furthermore, there is evidence for tidally-controlled intrusions of relatively warm ocean water by up to 16 km below grounded ice during (high) spring tides in the Amery ice shelf (Chen et al., 2023) and by 6–12 km in the Thwaites glacier (Rignot et al., 2024). Similarly, the GL migrates over a zone of 2–6 km in Petermann Glacier in the northwest of Greenland (Ciraci et al., 2023) and over almost 3 km in Jakobshavn Isbræ in the west of Greenland (Kim et al., 2024). These migrations of the GL lead to the definition of a region called the grounding zone (GZ; Parizek, 2024; Rignot et al., 2024). The intrusion of salty ocean water beneath the ice



sheet leads to ice melt by delivering high amounts of ocean heat to zones where, on average, ice can be considered grounded.
60 Melting rates of as much as 50 m yr^{-1} have been found within the GZ, yielding much higher values than those observed in the adjacent ice shelf (Milillo et al., 2019; Rignot et al., 2024).

Grounding-line retreat can easily be triggered by basal melting in its vicinity in response to oceanic thermal forcing (Arthern and Williams, 2017; Reese et al., 2018; Seroussi and Morlighem, 2018; Parizek, 2024). During the past decade, allowing for submarine melting at even partially floating grid points was thought to lead to an overestimated GL retreat in response to
65 oceanic forcing (Seroussi and Morlighem, 2018; Robel et al., 2022). However, in light of the evidence above, this view is changing. Several studies have actually linked the difficulties of current ice-sheet models to reproduce features such as the ice loss during recent decades or the sea-level highstands from previous interglacials with the lack of submarine melting within the GZ (Chen et al., 2023; Bradley and Hewitt, 2024; Rignot et al., 2024). Obviously, an increased model sensitivity would have implications for future ice-volume and sea-level projections.

70 In view of these results, a revision in the representation of submarine melting in ice-sheet models has been proposed by adopting schemes that include melting upstream of the GL. Gadi et al. (2023) used a very high-resolution two-dimensional ocean-ice model to calculate submarine melt rates as a function of the grounding-zone length and ocean thermal forcing. Melt rates were found to increase sub-linearly with the grounding-zone length. However, the grounding-zone length in this study was treated as a tunable parameter rather than as a variable predicted by the model.

75 Wilson et al. (2020) developed a theory of layered seawater intrusion in laterally-confined subglacial channels. Robel et al. (2022) generalized this theory to include subglacial hydrology as a macroporous water sheet over impermeable beds and as microporous Darcy flow through permeable till. Seawater intrusion upstream of the GL was predicted to be limited to just several metres for permeable till, but capable of reaching tens of kilometres over flat or retrograde impermeable beds. In the first case, projections of marine ice-sheet volume loss increased by 10–50% (Robel et al., 2022); for kilometric-scale intrusions,
80 projected ice-volume loss can more than double. Again, the grounding-zone length was treated as a tunable parameter.

Robel et al. (2022) derived an expression for the scale of the intrusion length, which was found to depend on the presence of subglacial channels, the nature of the bed (i.e. deformable bed or till versus hard bed), the porosity, the bed topography (slope), the regime of basal hydrology, the thickness of the seawater layer under the ice, the upstream velocity of the subglacial discharge, and the degree of obstruction by obstacles. Observational studies have confirmed many of these dependencies and
85 included others such as the ice-flow velocity (Brancato et al., 2020; Milillo et al., 2022; Chen et al., 2023; Zhu et al., 2025). Many of these variables are, however, not straight-forward observables. Furthermore, their representation in state-of-the-art continental-scale ice-sheet models remains challenging, especially when it comes to subglacial hydrology. Robel et al. (2022) introduced an equation that represents the melt upstream from the GL as being proportional to the ocean-induced basal melting at the GL, where upstream melting decreases linearly to zero at a specified distance L upstream (see Eq. 22 therein). This
90 approach allows for a first-order representation of melt due to tidal intrusions. It is clear though, that L may vary spatially and would depend on the factors listed above. A critical issue is therefore how to determine the length of the GZ with such an approach.



In this study, we propose a simple parameterization of submarine melting that accounts for the length and location of the GZ based on topographical features. This parameterization is dependent on a single parameter that can be estimated from the observational evidence. Melting is then calculated as a spatially weighted melt distribution between grounded and floating ice. To assess the influence of this parameterization, we investigate the sensitivity of the AIS response to the length of the GZ under a future high-emission scenario with the ice-sheet model Yelmo.

This work is structured as follows. In Sect. 2 the ice-sheet model used and the experimental setup are described, together with the description of the parameterization. In Sect. 3, the results of the experiments are presented with special emphasis on the effects of ocean warming and GZ expansion on sea-level contributions. In Sect. 4 we discuss these results comparing them with similar studies. Finally in Sect. 5 conclusions from this study are drawn.

2 Methodology

2.1 Ice-sheet model setup

In this study, we use the Yelmo ice-sheet model (Robinson et al., 2020) with a horizontal resolution of 16 km (grid of 381×381 cells) and 10 vertical layers. Yelmo has been tested in benchmark experiments, e.g. EISMINT and MISMIP (Robinson et al., 2020). It has been applied in different domains, including the Laurentide Ice Sheet (Moreno-Parada et al., 2023), the Greenland Ice Sheet (Bochow et al., 2023; Gutiérrez-González et al., 2025), and the AIS (Blasco et al., 2021; Juarez-Martinez et al., 2024), and participated in ISMIP6-2300 (Seroussi et al., 2024).

All experiments presented assume that ice dynamics follow Glen's flow law, relating stress deviatoric tensors with stress rate tensors through an exponent n , defined for this study as 3, and a rate factor $A = EA(T')$ which follows an Arrhenius law. This law is dependent on the temperature relative to the pressure melting point T' , and an enhancement factor E , that takes into account different deformation regimes. These enhancement factors have been chosen as 1.0, 1.0, and 0.7 for the shear, stream, and shelf regions, respectively (Greve and Blatter, 2009). The velocity field is computed using the higher-order depth-integrated viscosity approximation (DIVA; Robinson et al., 2022). Basal stress τ_b is implemented as a regularized Coulomb power law (Joughin et al., 2019), given in terms of the basal velocity $\mathbf{u}_b = (u_b, v_b)$ as:

$$\tau_b = -c_f N \left(\frac{|\mathbf{u}_b|}{|\mathbf{u}_b| + u_0} \right)^q \frac{\mathbf{u}_b}{|\mathbf{u}_b|} \quad (1)$$

with the exponent $q = 0.2$, and $u_0 = 100 \text{ m yr}^{-1}$ being an empirical threshold speed below and above which viscous and Coulomb friction are obtained, respectively (Zoet and Iverson, 2020). The dimensionless parameter c_f represents the frictional properties of the bedrock and is optimized during the spinup as by Juarez-Martinez et al. (2024). The effective pressure N depends on the basal hydrology, which follows from a local energy balance and a fixed till drainage rate (Bueller and van Pelt, 2015):



$$N = \min \left\{ P_o, N_0 \left[\left(\frac{\delta P_o}{N_0} \right)^s 10^{\frac{e_0}{C_c} (1-s)} \right] \right\} \quad (2)$$

where $N_0 = 1000$ Pa is the reference effective pressure, P_o is the overburden pressure of ice, $e_0 = 0.69$ is the reference void ratio (for $N = N_0$), $s = H_w/H_{w,\max}$ is the ratio between the height of basal water content and the maximum height allowed (2 m in this case) and $C_c = 0.12$ is the till compressibility. Also, the fraction of overburden pressure for saturated till is set to $\delta = 0.8$. Calving is parameterized through the von Mises criterion (Lipscomb et al., 2019).

Submarine melting is parameterized through the generalized non-local basal melt parameterization described by Jourdain et al. (2020) and used within ISMIP6 (Seroussi et al., 2020). This parameterization takes into account not only the local thermal forcing, but also the effects of the average forcing over the cavity beneath a given ice shelf. The sub-shelf basal melting of floating ice $\dot{b}_f(x, y)$ is given by:

$$\dot{b}_f(x, y) = \gamma_0 \left(\frac{\rho_{sw} c_{pw}}{\rho_i L_f} \right)^2 (T_F(x, y, z_{draft}) + \delta T_{sector}) | \langle T_F \rangle_{draft \in sector} + \delta T_{sector} | \quad (3)$$

where $T_F(x, y, z_{draft})$ is the thermal forcing (the oceanic temperature relative to the pressure melting point, dependent on salinity) at the ice-ocean interface, with z_{draft} being the thickness of the ice shelf, ρ_{sw} is the density of ocean water, L_i the latent heat of fusion of ice and c_{po} the specific heat of the ocean water. δT_{sector} is a temperature correction to reproduce the observed ice thickness (see Section 2.3) and $\langle T_F \rangle_{draft \in sector}$ represents the thermal forcing averaged over all ice shelves contained in each of the 18 drainage basins in which the Antarctic domain is divided (Jourdain et al., 2020). The parameter γ_0 is a heat-exchange factor with a value of 14500 m yr^{-1} corresponding to the medium value used in the ISMIP6 protocol (Seroussi et al., 2020).

Yelmo is coupled to FastIsostasy, a 2D Glacial Isostatic Adjustment (GIA) model that accounts for the lateral variability of the solid Earth structure and computes the spatially heterogeneous sea-surface elevation resulting from gravitational anomalies (Swierczek-Jereczek et al., 2024). For our simulations, we consider two layers for representing the Earth's inner structure: the lithosphere and the mantle, with densities of 3200 kg m^{-3} and 3400 kg m^{-3} , respectively. The laterally-variable rheology (lithospheric thickness and mantle viscosity) and Earth structure were obtained from Lloyd et al. (2024). The barystatic sea level evolves according to the AIS topography, as described by Goelzer et al. (2020).

2.2 Parameterization of subgrid tidal intrusion

Leguy et al. (2021) introduced the partial melt subgrid parameterization (PMP) to account for basal melting at partially floating grid cells containing the GL (see also Seroussi and Morlighem, 2018). Here, we introduce a modification of PMP, hereafter the Partial Melt Parameterization with Tides (PMPT), to account for submarine melting resulting from tidal water intrusions under grounded ice. With this approach, we do not intend to represent vertical motion of tides, but rather the extent of the tidal intrusions. Tsai and Gudmundsson (2015) demonstrated that grounding-line migration is not proportional to the height of tides, but rather nonlinear and asymmetrical, favoring upstream migration. In addition, Rosier and Gudmundsson (2020) and



Zhu et al. (2025) demonstrated that vertical motion of between 2 and 3 metres can make the GL migrate several kilometers horizontally.

In the PMPT approach, we make the important assumption that the intrusion distance upstream from the grounding line, L , can be expected to be inversely proportional to the along-flow gradient of ice thickness above flotation, i.e.,

$$L \propto \left(\frac{\partial H_{af}}{\partial x} \right)^{-1} \quad (4)$$

where $H_{af} = H - \frac{\rho_{sw}}{\rho_i} \max(z_{sl} - z_{bed}, 0)$ is the ice height above flotation, H is the ice thickness, z_{sl} is the sea level, z_{bed} is the bedrock elevation and x can be considered the coordinate along a flowline from the GL ($x = 0$) increasing in the upstream direction. By definition $H_{af} \rightarrow 0$ as $x \rightarrow 0$. In other words, we assume that the intrusion length is small when H_{af} increases rapidly moving upstream, and the intrusion length is large when H_{af} increases slowly moving upstream (Fig. 1). Such an assumption seems to be consistent with theory (Robel et al., 2022) and, as we will show, with observations in the broad sense. This relationship implies that we can define a threshold ice height above flotation, H_t , that corresponds to the intrusion length, $H_t = H_{af}(x = L)$.

In this way, we can avoid defining the intrusion length directly, since this is challenging to represent in the model, while H_{af} is a variable that is readily available. Thus we can define a weighting function for the fraction of ocean-driven melt to be applied as:

$$w_f = 1 - \frac{H_{af}}{H_t}, \quad (5)$$

which is valid for $0 < H_{af} < H_t$. With this equation, the amount of melting reduces linearly, as $H_{af} \rightarrow H_t$. To calculate the basal melting at a given location then, we use the following equation:

$$\dot{b} = \begin{cases} \dot{b}_g, & \text{if } H_{af} \geq H_t, \\ \dot{b}_f, & \text{if } H_{af} \leq 0, \\ (1 - w_f)\dot{b}_g + w_f\dot{b}_f, & \text{if } 0 < H_{af} < H_t. \end{cases} \quad (6)$$

where \dot{b}_f is the basal melting for floating ice as introduced in Eq. 3 and \dot{b}_g denotes basal melting for grounded ice resulting from basal friction heat and geothermal heat flow. The melt applied at the GZ is therefore determined as a weighted average between \dot{b}_g and \dot{b}_f , which depends on H_{af} at that point.

In the following study, we have imposed a spatially constant value of H_t , as we believe that through this formulation H_t represents some of the first-order spatial variation in intrusion length that would be due to characteristics of the bedrock slope and ice thickness. Nonetheless, we note that it would also be possible to refine H_t into a spatially variable field as desired.

In the model, we calculate basal melting at the subgrid scale first by bilinearly interpolating H_{af} to a subgrid of $M \times M$ points, where here we set $M = 15$. Basal melting \dot{b} , is then calculated at each subgrid point via Eq. 6. Finally the basal melt for the current grid cell is determined as the mean of the subgrid points, $\dot{b} = \frac{1}{M \cdot M} \sum_j \dot{b}_j$.

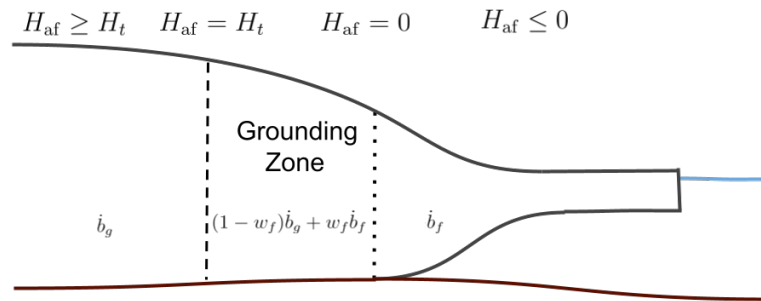


Figure 1. Schematic representation of a marine ice-sheet section to illustrate the PMPT parameterization. The slope of the ice surface and bedrock determine the distance upstream of the GL (corresponding to $H_{af} = 0$) at which $H_{af} = H_t$ and therefore the extent of tidal seawater intrusion or grounding-zone length.

180 Note that if H_t is set to zero, this implies that tidal intrusions are not considered, and the approach will reproduce the standard PMP melt based on the fraction of the grid cell that is floating. Throughout the paper, we consider the case of $H_t = 0$ as the reference case, and we compare the impact of considering tidal intrusion with values of $H_t > 0$.

To estimate a reasonable range for the parameter values H_t , we use recent observations of the GZ for several regions obtained through differential radar interferometry (DInSAR) in the Amery ice shelf (Chen et al., 2023; Zhu et al., 2025), the Thwaites
 185 Glacier (Rignot et al., 2024), Berry Glacier (Chen et al., 2025); and three glaciers within the EAIS: Totten Glacier, Rennick Glacier, and Moscow University Ice Shelf (Ross et al., 2025). In Fig. 2, these regions are shown with isolines of H_{af} overlain as determined from the Bedmap3 ice and bedrock topography (Pritchard et al., 2025). In all cases, the observed GZ is found to lie well within $H_{af} < 250$ m. The different datasets have a distribution clearly oriented towards positive values (Table A1), suggesting that grounding-zone extents are well above zero, in the range $H_t = [15, 130]$ m (Fig. 2).

190 An exception is the Amery ice shelf (Figs. 2f and A1), where our parameterization fails to represent the observed GZ regardless of the H_t value. We attribute this mismatch to a likely bias in the topography dataset where the bedrock uncertainty reaches more than 250 m (Pritchard et al., 2025). Therefore, leaving aside this case, our parameterization broadly captures the observed GZs for which DInSAR data and reasonably good estimates of the bedrock topography are available. We have also made a similar comparison for two Greenland glaciers (Fig. A2) that supports our approach: Petermann Glacier (Ciraci et al.,
 195 2023) and Jakobshavn Isbrae (Kim et al., 2024).

2.3 Experimental setup

For each value of H_t selected for this work (see below), a 10-kyr-long spinup was obtained by forcing Yelmo with monthly values of the atmospheric fields (surface mass balance, SMB, and 2m air temperature) from the Regional Atmospheric Climate Model (RACMO2.3; Van Wessem et al., 2014) forced by the ERA-Interim reanalysis (Dee et al., 2011), averaged over the

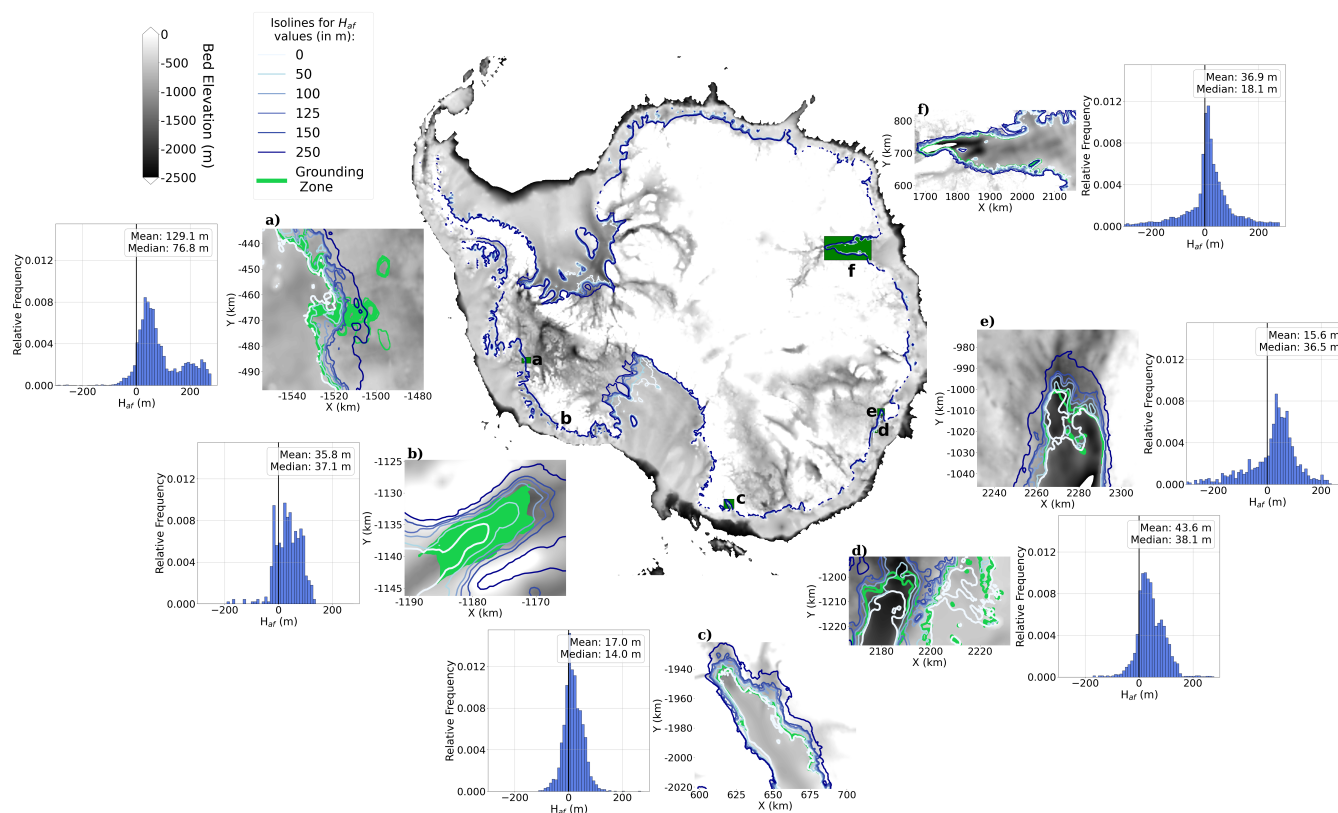


Figure 2. Observational estimates of the GZ for different regions compared with isolines of thickness above flotation. Rectangles with letters a-f delimit the extension of the different regions of the insets, for which the observational GZ obtained through DInSAR from different studies is shown in green: a) Thwaites Glacier (Rignot et al., 2024), b) Berry Glacier (Chen et al., 2025), c) Rennick Glacier (Ross et al., 2025), d) Moscow University Glacier (Ross et al., 2025), e) Totten Glacier (Ross et al., 2025) and f) Amery Ice Shelf (Zhu et al., 2025). The isolines of thickness above flotation, H_{af} , are calculated from the Bedmap3 dataset (Pritchard et al., 2025) with a resolution of 500 m. Grayscale shading shows the bedrock topography. Next to each panel, histograms of the H_{af} (m) values are shown corresponding to the data points contained within the GZ. Mean and median values are indicated in each panel.



200 period 1979–2022. For the ocean, the present-day climatology (temperature and salinity fields) constructed by Jourdain et al. (2020) for ISMIP6 from existing observational datasets was used. The basal friction field was optimized by tuning the friction coefficient c_f over the first 6 kyr so that the modelled ice thickness matches the present-day observed ice thickness, from the BedMachine Antarctica V2 dataset (Morlighem et al., 2020), also representing the initial configuration of the ice sheet before the spin-up is performed. To make this optimization for c_f , we use the differential equation from Lipscomb et al. (2021):

$$205 \quad \frac{dc_f}{dt} = -\frac{c_f}{H_0} \left[\frac{H - H_{obs}}{\tau_c} + 2\frac{dH}{dt} + \frac{H_0}{20} \frac{\log(c_f/c_{f,target})}{\tau_c} \right] \quad (7)$$

where $H_0 = 100$ m and $\tau_c = 500$ years are constants for scaling in ice thickness and relaxation time respectively, and $c_{f,target}$ is a target for c_f defined as a function of elevation following Winkelmann et al. (2011). The last term of the equation ensures that in places where the optimization is less successful, the value of c_f does not saturate to an extreme value.

The same optimization process is carried out for the oceanic temperature correction δT , with a minimum and maximum
210 allowed correction of -1 K and 1 K, respectively. For the last 4 kyr, these two optimized fields are held constant, and the simulation equilibrates towards a steady state. The location of the simulated traditional GL (corresponding to $H_{af} = 0$) at the end of the spinup varies slightly depending on the value of H_t , but is very similar in all cases (Fig. A3). Accordingly, the errors in the initial states as compared to the observations are very close regardless of the value of H_t , so that they all correspond to plausible initial states (Figs. A4 and A5).

215 Starting from these spinups we carried out projections of the AIS from 2015 to 3000. Until 2300, we used the output of the CESM2-WACCM General Circulation Model (GCM) under the SSP5-8.5 scenario, which provides annual SMB anomalies with respect to the reference year (here 2015) based on the precipitation, runoff, evaporation, and sublimation calculated by the GCM. These anomalies are added to the reference SMB used during the spinup. The oceanic annual mean thermal forcing is derived from the GCM output as described by Jourdain et al. (2020). From 2300 to 3000 the forcing is kept constant and equal
220 to the average of the period 2291–2300. This corresponds to a strong oceanic thermal forcing, reaching up to 8 K by the end of the period (Fig. A6).

We assess the sensitivity of the projected Antarctic SLC to the extent of the tidal water intrusion by varying H_t within [0, 150] m at 25-m intervals. The case of $H_t = 0$ corresponds to our default model setup when tides are not considered, which serves as a basis for understanding the impact of including water intrusions into the GZ.

225 A control run with no anomaly forcing is also carried out for each H_t value. These control runs show negligible trends, varying less than 12 cm SLE over 1000 years in all cases (Fig. 3).

3 Results

Figure 3 shows the projected SLC of the AIS for the different values of the tidal intrusion parameter. The total SLC clearly increases with increasing H_t . The SLC progressively grows until 2300 where it ranges from 2.0 to 2.5 m SLE for the estimated
230 lower ($H_t = 0$ m) and higher ($H_t = 150$ m) limits, respectively (Table A2). Then, the SLC starts to increase more slowly. By

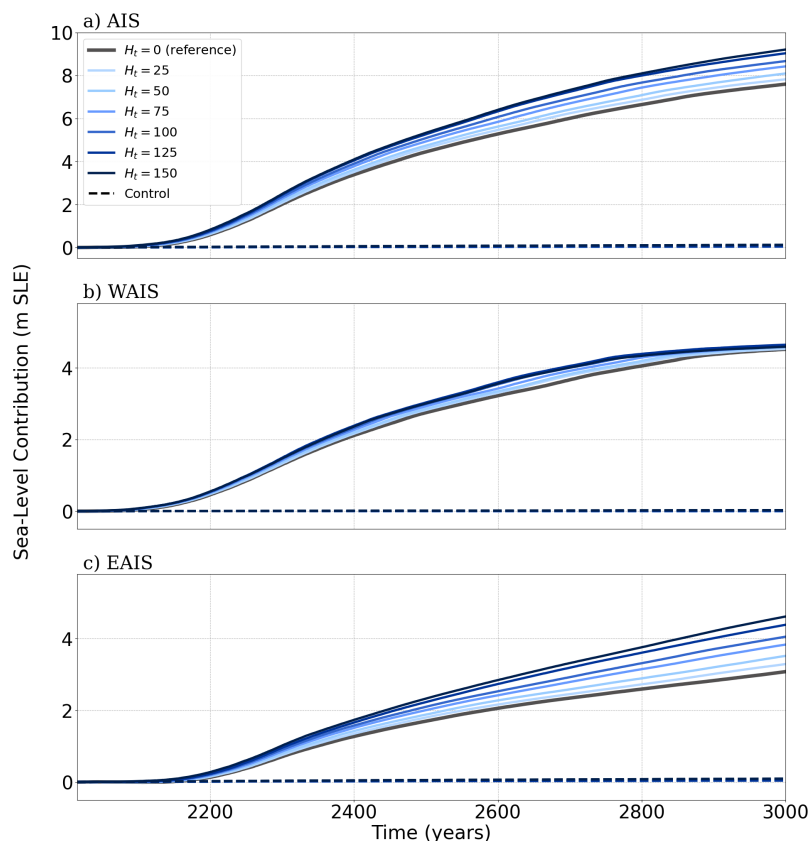


Figure 3. SLC (relative to 2015, m SLE) for the different values of H_t (in m) used. In a) for the whole AIS, in b) for the WAIS, and in c) for the EAIS. Dashed lines represent the control simulations corresponding to the different values of H_t , overlapping as variations are very small during the simulation period.

3000, it ranges between 7.6 and 9.2 m SLE, for the lower and higher limit, respectively. The spread, therefore, grows over time, reaching roughly 1.6 m SLE (or 21 %) by the end of the simulation.

The SLC from the WAIS follows a similar evolution (Fig. 3b). At 2300, it yields about 1.5 m SLE. At 3000, however, it shows no sensitivity to tidal intrusion, reaching about 4.5 m SLE for all H_t values. The reason for this behaviour is essentially due to saturation in mass loss in the region, since by this point, the WAIS has collapsed entirely. The East-Antarctic SLC in contrast shows a very large spread. By 2300, its contribution ranges between 0.7 and 1.0 m SLE and, by 3000, between 3.1 and 4.6 m SLE, in both cases for the lower and higher tidal-intrusion estimated limits, respectively (Table A2). The SLC increase attributable exclusively to the inclusion of tidal melt varies between 3 % and 21 % for $H_t = 25$ m and $H_t = 150$ m, respectively, relative to the reference case where $H_t = 0$ m (Table A3).

The value of H_t affects the SLC through its effect on basal melting within the GZ. Basal melting is the weighted sum of the contributions for grounded and floating ice (Eq. 3), with the latter typically much larger in magnitude. Inspecting cumulative



basal melting at early stages allows us to identify the effect of enhanced intrusion in basal melting within the GZ before the forcing has caused a significant retreat or significantly affected the ice flow and thereby basal melting due to frictional heat. Increasing H_t leads to larger basal melting as a result of larger intrusion (Fig. A7), which is most clearly seen in the
245 Ronne-Filchner ice shelf. The intrusion length therefore controls the amount and extent of basal melting within the GZ at early stages.

The enhanced basal melting contributes to increased discharge and further ice thinning (Fig. 4), producing an acceleration of ice streams and increasing ice surface velocities (Fig. 5). Although the imposed forcing (Fig. A8) is substantial and contributes to the system's response, the value of H_t is the primary factor controlling the temporal evolution of spatial anomalies in ice
250 thickness and ice surface velocities relative to the reference case ($H_t = 0$ m). By 2300, most of the ice-mass loss takes place in the WAIS, where the basal melting is the largest. The Antarctic Peninsula almost becomes detached from the rest of the ice sheet, and the GZ shows a general retreat towards the interior, notably at the western limit of the Ross ice shelf. The grounding-zone retreat enhances the acceleration of ice streams and, over time, allows anomalies to extend hundreds of kilometres inland with respect to the reference case.

255 In the eastern part, the Recovery basin also shows substantial grounding-line retreat, ice-stream acceleration, and ice loss. In the EAIS, the retreat of the GZ is much more limited in comparison, although the basal melting anomalies in both areas are, however, comparable (Fig. A9). Accordingly, the ice-thickness and velocity anomalies clearly increase with increasing H_t . Ice only increases in a small region near the Amundsen Sea in response to lower velocities, but these anomalies revert their sign as the simulation progresses in time, and ice loss both in the WAIS and the EAIS intensifies and spreads farther into the ice-sheet
260 interior. Again, the retreat of the GZ is faster with increasing H_t values, in response to the increase of basal melting anomalies. By 2500, it is predominantly concentrated in the Amundsen Sea and the Ross Ice Shelf. By 3000, the high oceanic thermal forcing (Fig. A8) eventually leads to an almost complete collapse of the WAIS for all H_t values. This explains the almost zero spread in the West-Antarctic SLC for CESM2-WACCM shown in Fig. 3b. In the EAIS, George V and Wilkes Land now show a larger ice loss than the Recovery Basin due to its stronger marine character (Fig. A8).

265 4 Discussion

Observational evidence of significant tidal intrusions upstream of the Antarctic GL challenges the paradigm of strongly limited basal melting beyond the GL, prevalent in current modelling of the AIS. Tidal intrusions may significantly influence GL behaviour and ice dynamics, in particular, the future evolution of the AIS. These processes, however, have not been explicitly accounted for in large-scale ice-sheet projections, including modelling frameworks such as ISMIP6.

270 Rignot et al. (2024) suggested that models with grounding-zone lengths of several kilometres should produce higher projections of glacier loss, with SLC increasing by a factor of two for very high melting. In the long term, our results show a general trend of an increase in SLC with increasing tidal penetration, approximately by 20%, and larger in the short and mid term.

The sensitivity of the SLC in this case is entirely due to the spread in the EAIS contribution. The WAIS response in this scenario and GCM model is not sensitive to the strength of tidal penetration at the end of the simulation period. This is a

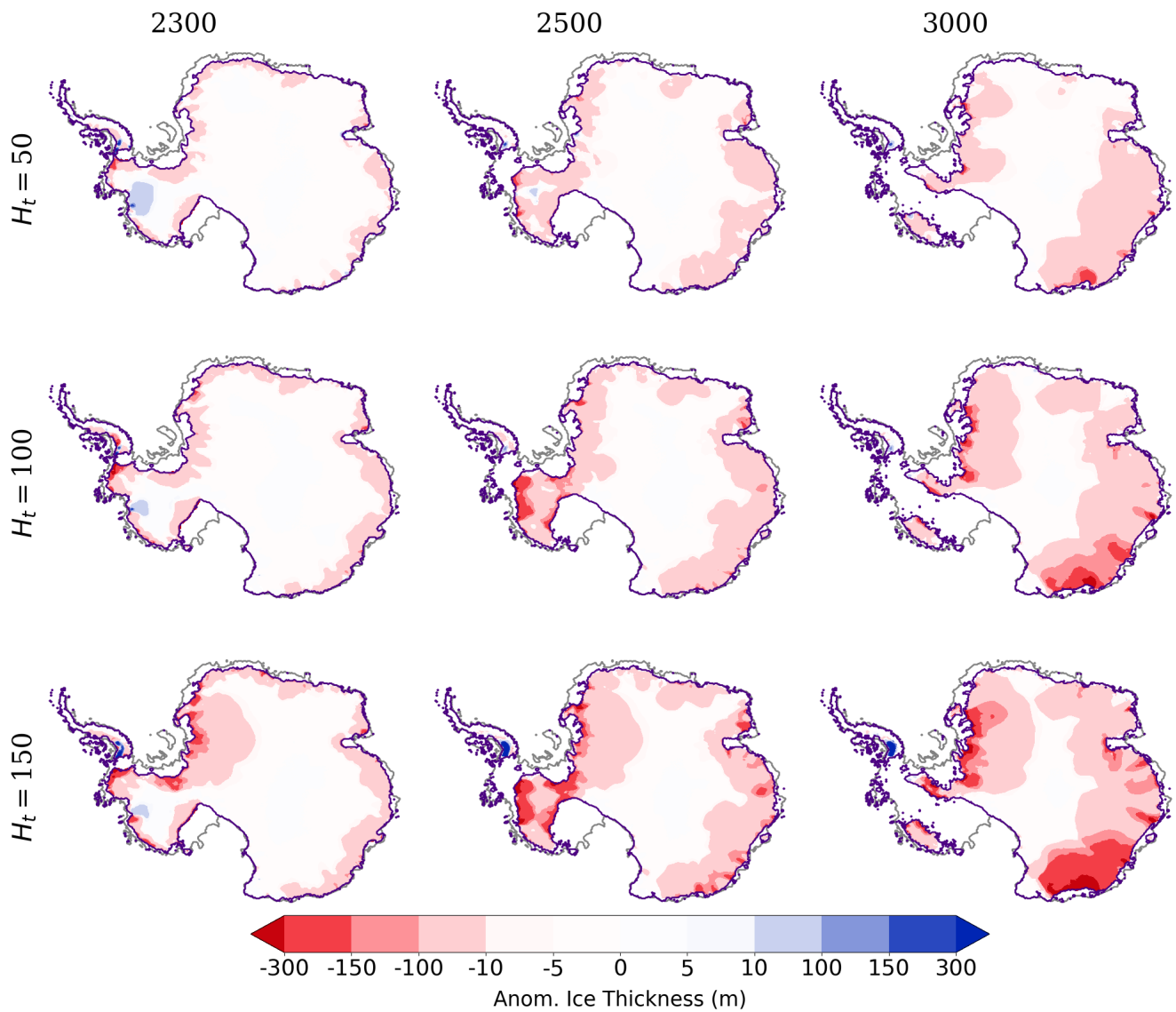


Figure 4. Ice thickness anomalies (m) for the different values of H_t at different timesteps with respect to the case where $H_t = 0$ m for the experiments with CESM2-WACCM (SSP5-8.5). The gray and purple lines represent the initial and evolving GL, respectively (defined as $H_{at} = 0$).

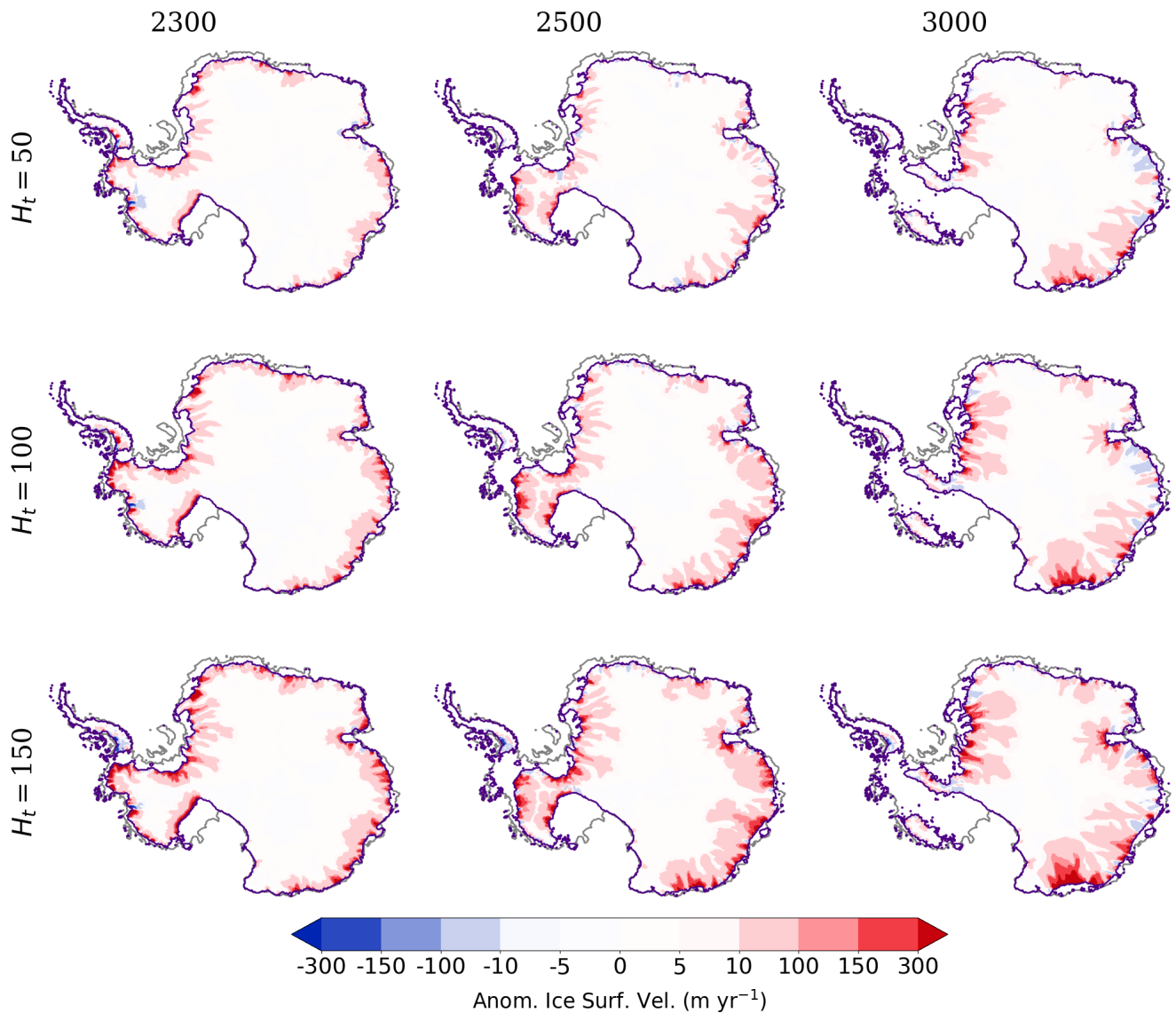


Figure 5. Ice surface velocity anomalies (m yr⁻¹) for the different values of H_t at different timesteps with respect to the case where $H_t = 0$ m for the experiments with CESM2-WACCM (SSP5-8.5). The gray and purple lines represent the initial and evolving GL, respectively (defined as $H_{af} = 0$).



275 consequence of the strong forcing in CESM-WACCM under SSP5-8.5, which causes its collapse for all H_t values, yielding
an SLC of around 4.5 m SLE by year 3000. However, H_t controls the timing of this collapse. For instance, with $H_t = 50$ m,
the level of 4 m SLE is reached at year 2755, and with $H_t = 150$ m already in the year 2696. Meanwhile, in the short term,
we barely find any sensitivity with respect to the strength of tidal penetration. Therefore, it is unclear at this point whether our
parameterization would be able to account for a larger current ice-mass loss. Investigating this issue would require mimicking
280 the exact oceanic forcing during the recent decades, including its variability, which is outside the scope of our analysis.

The simulated mass gain until year 2300 in the adjacent areas of the Amundsen Sea Embayment (Fig. 4) may appear
counterintuitive, given the region's well-known sensitivity to ocean forcing. This is explained by the difference in ice thickness
at the beginning of the simulations which happens to give $H_t = 0$ an underestimation in ice thickness with respect to other
values of H_t , due to slightly greater temperatures at the end of the spin-up. Nevertheless, this mass gain is relative to $H_t = 0$,
285 small and transient and does not contradict the long-term vulnerability of the region which partially collapse in 2500.

Our parameterization for basal melting goes in line with the suggestion of Robel et al. (2022) of dynamically calculating
the grounding-zone width. In our case, this length solely depends on the bed and ice thickness slopes. Chen et al. (2023) and
Zhu et al. (2025) showed that the width of the GZ decreases with increasing slopes of the ice thickness, and most notably the
bedrock, following almost an exponential law. Our parameterization captures this to a certain extent through its dependency on
290 these topographical features. Ross et al. (2025) further showed a linear dependency with ice velocity on regions with thicker
glaciers and faster ice flows, with the elasticity of ice playing a key role in the physical process.

Our approach is simple to understand and investigate, easy to implement, and does not involve any additional computational
costs. However, it does not take into account layered seawater intrusion that can take place when subglacial water is discharged
to the ocean close to the GZ (MacGregor et al., 2011; Horgan et al., 2013; Milillo et al., 2019; Wilson et al., 2020; Robel et al.,
295 2022). Including this effect would require the inclusion of a comprehensive subglacial hydrology module, which is absent in
most ice-sheet models and represents a large source of uncertainty (Robel et al., 2022). A more sophisticated treatment of
seawater intrusion in ice-sheet models would also include its dependency on the local bed type (hard or soft). However, the
extent of soft and hard beds below the Greenland and Antarctic ice sheets remains somewhat unknown.

We have calibrated the parameter controlling the length of intrusion using grounding-zone extensions as diagnosed from
300 DInSAR in AIS glaciers, such as Amery (Chen et al., 2023; Zhu et al., 2025) and Thwaites (Rignot et al., 2024) in Antarctica.
We have also compared this approach in Greenland glaciers such as Petermann Glacier (Ciraci et al., 2023) and Jakobshavn
Isbrae (Kim et al., 2024). We have attempted to include as much observational evidence as possible. As new data might appear
in other glaciers, it should be possible to further test this parameterization in the future. We have imposed a spatially constant
value of H_t everywhere and tested the overall impact. However, it would also be possible to calibrate different values of H_t
305 for different regions.

Tidally controlled migrations of the GL occur on very short timescales that are not resolved here. High-resolution studies
solving the tidal cycle indicate that the resulting basal melting distribution along the GZ is highly asymmetric, and that sub-
marine melting is limited to around 72% of its length (Gadi et al., 2023). Additional studies should provide clues as to how to
translate high-frequency forcing into the mean basal melting required by ice-sheet models.



310 Regarding our experimental setup, model resolution is a key parameter. This is especially true at coarse resolutions, such as
the 16 km grid used here, that do not fully capture the dynamics of ice flow across the GL, even when subgrid or parameteriza-
tion schemes are applied (Williams et al., 2025). Coarse resolutions tend to produce higher estimates of sea-level contribution
compared to finer resolutions, thereby increasing the overall uncertainty.

In addition, regarding parameter sensitivity, the parameterization has thus far been evaluated using the parameter choices
315 specified in Section 2. The primary aim of this study is to isolate and assess the behaviour of the new formulation and its
dynamical impact on ice-sheet evolution. For this reason, we did not perform a systematic exploration of a broader parameter
space, as such an analysis would shift the focus away from evaluating the structure and performance of the parameterization
itself. A comprehensive sensitivity study would certainly be valuable and is a natural direction for future work, particularly to
better quantify uncertainty and assess robustness across different modelling configurations.

320 Finally, ocean tides do not only affect basal melting. Recently, it has also been shown that they influence the rate and timing
of calving and fractures in ice shelves (Marsh et al., 2025). These effects could also affect the response of ice sheets to a given
forcing and will possibly require a more comprehensive treatment, together with basal melting, in the future.

5 Conclusions

We introduce a new parameterization accounting for submarine melting within the grounding zone, which builds upon the
325 classical partial melting parameterization by explicitly incorporating the effects of tidal intrusion. Tidal intrusions correspond-
ing to regions with ice thickness above flotation of between 15 and 130 meters yield the best agreement with observations
of present-day grounding zones, indicating this may be a realistic and critical parameter range for future AIS models. This
approach reveals that the extent of assumed tidal penetration plays a substantial role in long-term sea-level projections. We
assessed its impact under one high-emission scenario with strong oceanic thermal forcing. Our simulations show that deeper
330 tidal intrusion can significantly amplify sea-level rise over a 1,000-year timescale, with a total sea-level contribution ranging
from 7.6 to 9.2 meters SLE. While the WAIS shows a near-total collapse regardless of the tidal penetration, the EAIS intro-
duces substantial uncertainty depending on the strength of tidal intrusion, with spreads exceeding 1.5 m SLE. In both cases, the
transient response of the ice sheet depends critically on the representation of tidally induced basal melting under the ice sheet.



Appendix A: Additional figures and tables

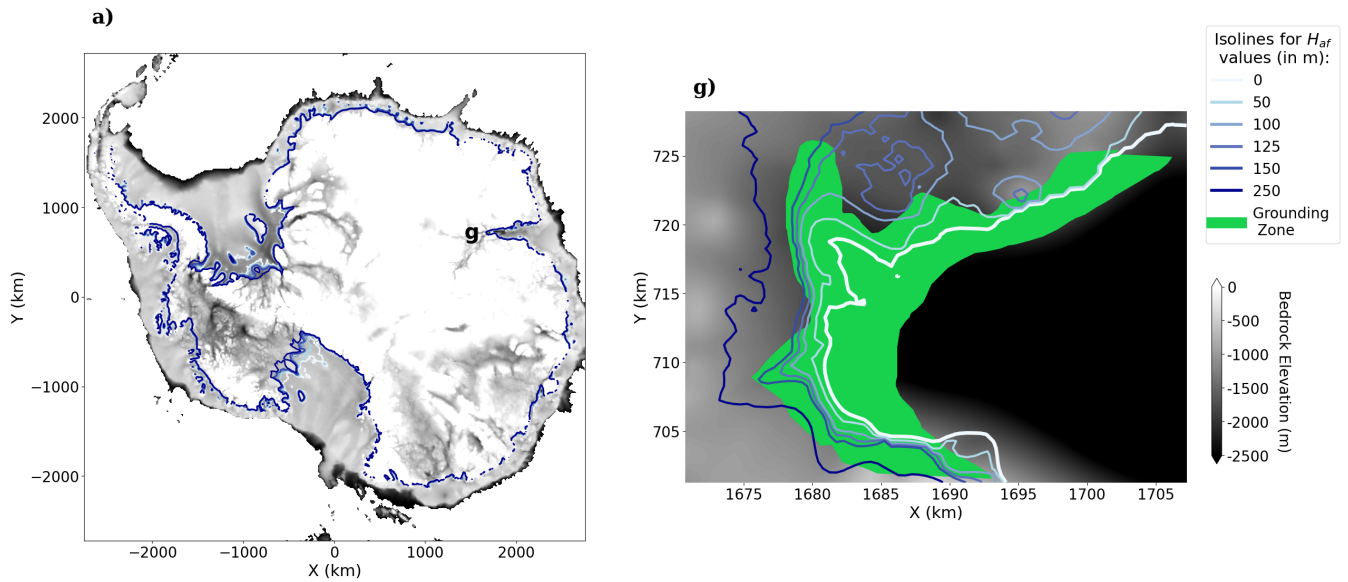


Figure A1. Same as Figure 2f, but considering the western most region of the Amery Ice Shelf (Chen et al., 2023). The mean and median for values are -39.0 m and 21.7 m, respectively.

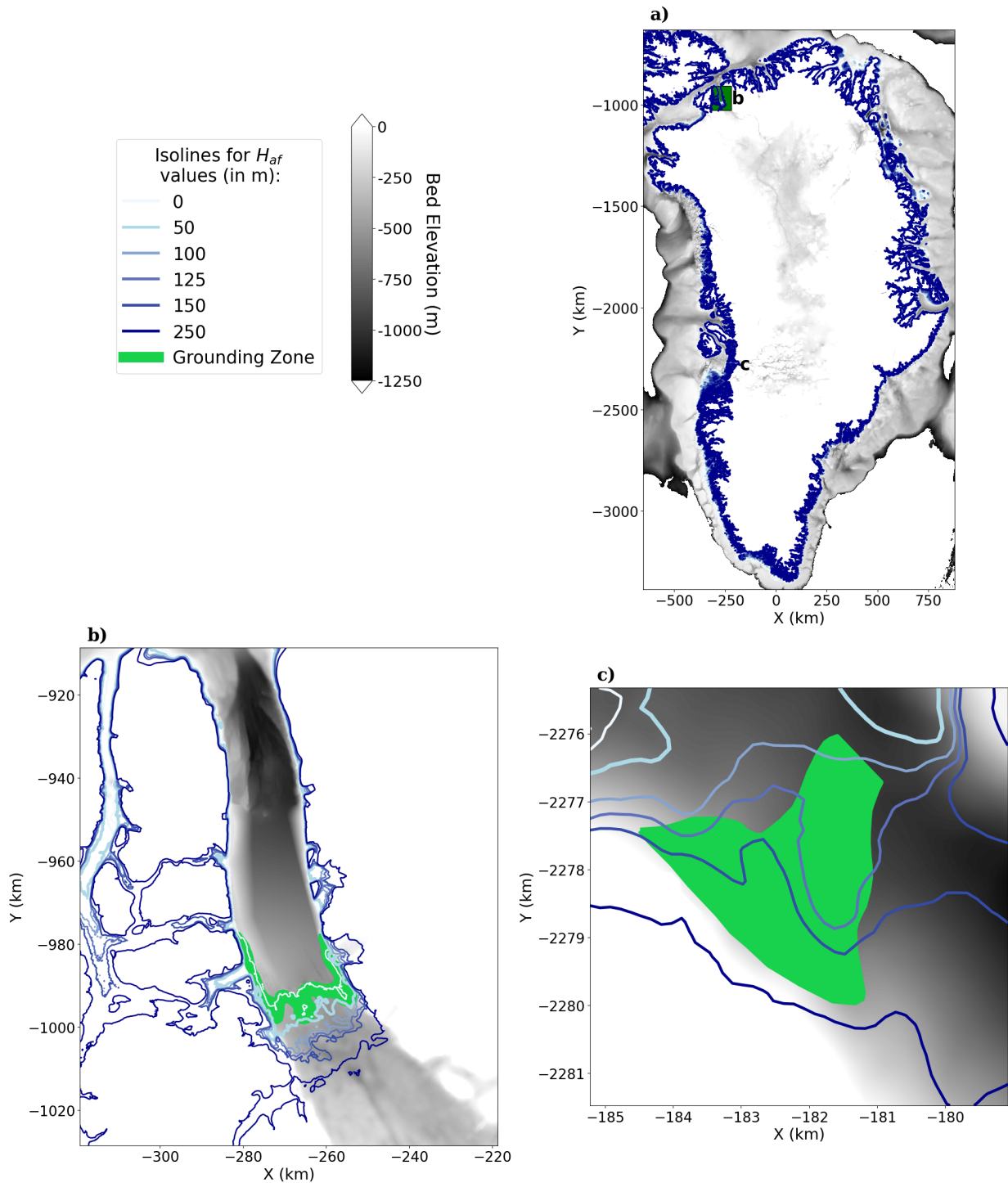


Figure A2. Same as Figure 2, but for two regions in Greenland (a), b) Petermann Glacier (Ciraci et al., 2023) and c) Jakobshavn Isbræ (Kim et al., 2024). Bathymetric dataset used from BedMachine Greenland V5 (Morlighem et al., 2022) with a resolution of 150 m.

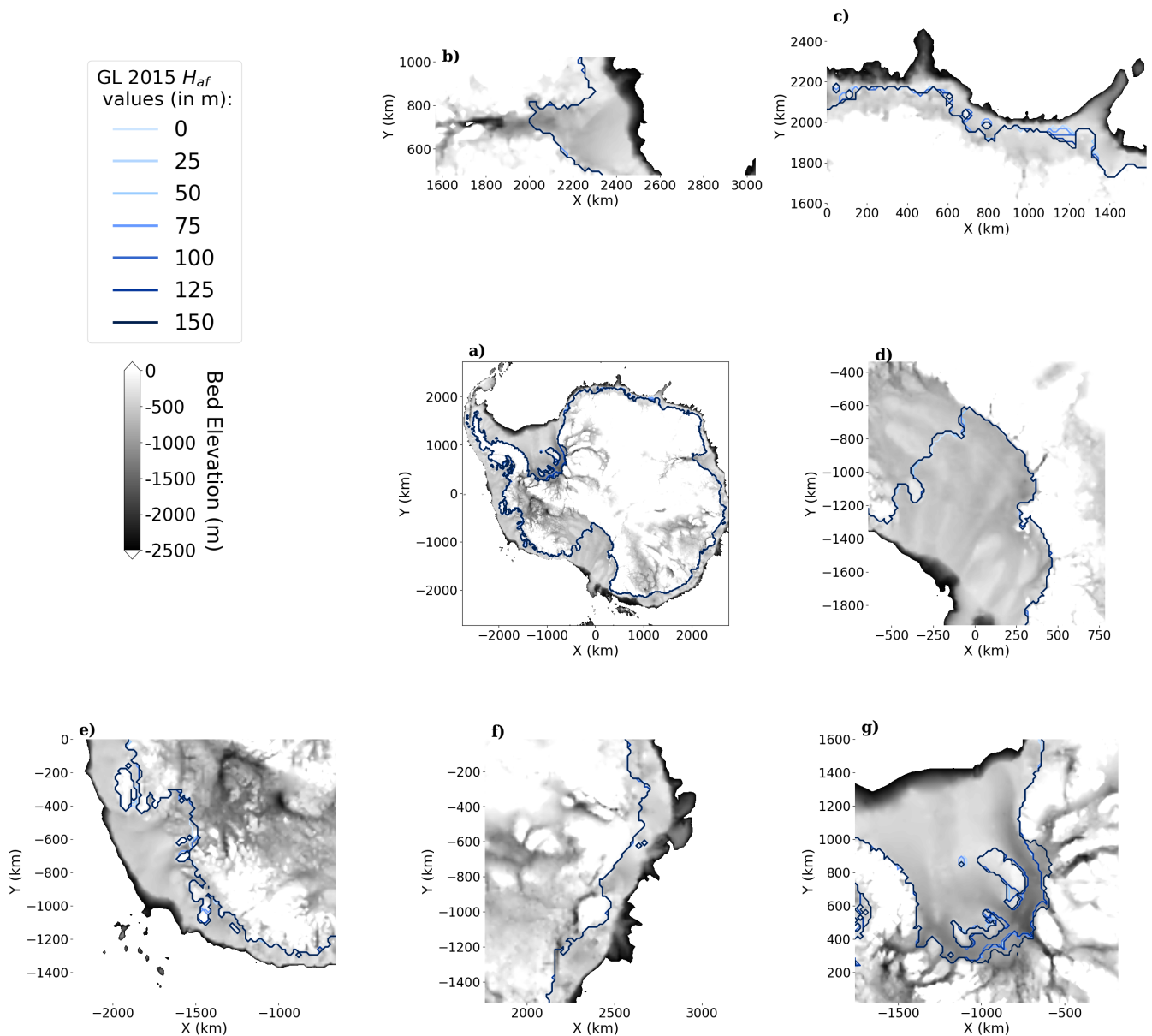


Figure A3. Grounding-line position (defined as $H_{af} = 0$) at the beginning of the projections for the different values of H_t used in the spinup runs. For the different subplots, particular regions of the AIS (a) have been zoomed in: b) Amery, c) Queen Maud Land, d) Ross Ice Shelf, e) Amundsen Sea Embayment, f) Wilkes Land and g) Ronne-Filchner Ice Shelf.

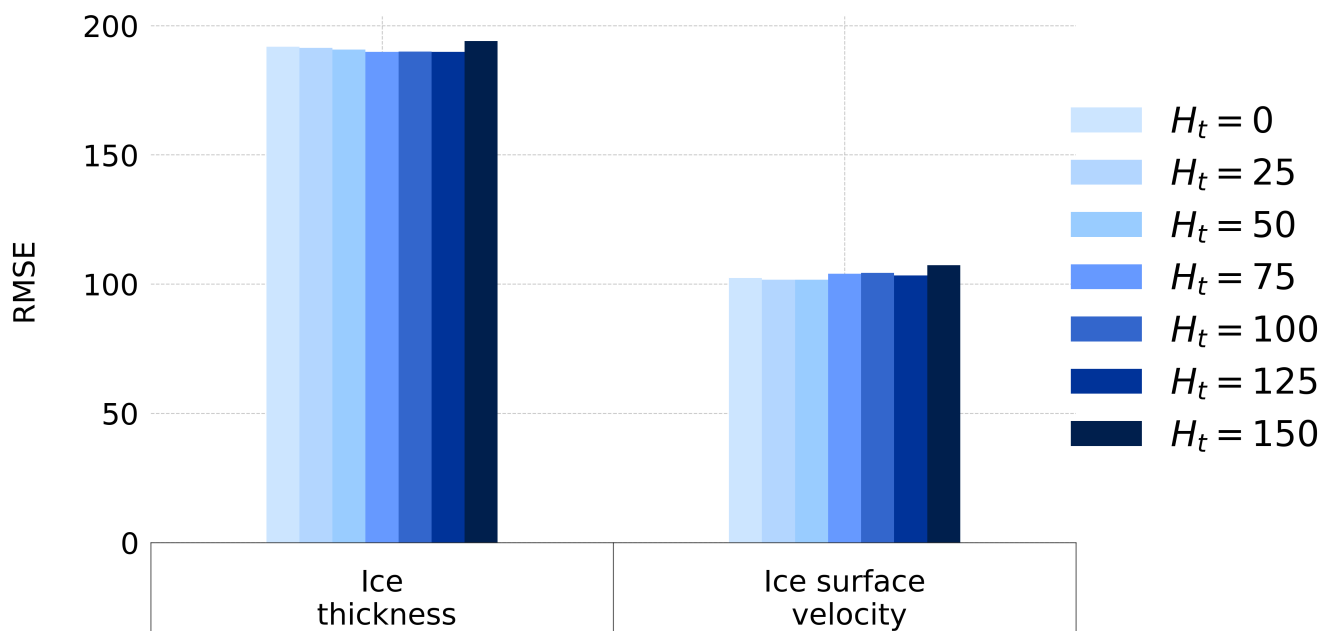


Figure A4. Root-mean-square error (RMSE) for ice thickness (in m) and ice-surface velocity (in myr^{-1}) between the start of the simulations in 2015 and observations. The different colours represent different values of H_t .

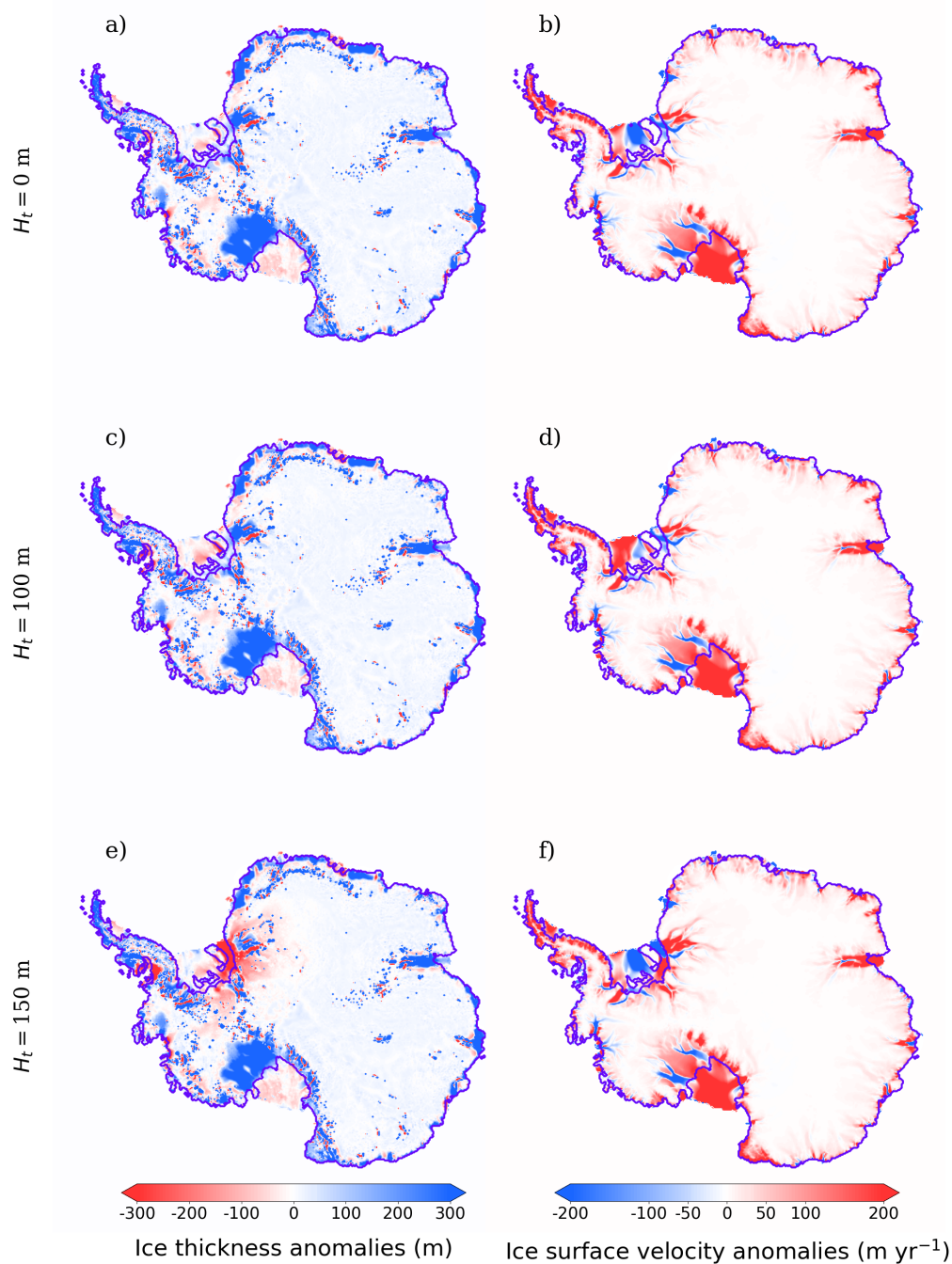


Figure A5. Errors in simulated ice thickness (in m) and surface velocity (in m yr^{-1}) at the end of the spinup for $H_t = 0$ m (a,b), $H_t = 100$ m (c,d) and $H_t = 150$ m (e,f), calculated as anomalies with respect to observations from the BedMachine Antarctica V2 dataset (Morlighem et al., 2020) and the Rignot et al. (2011) dataset, respectively. In purple, GL defined as $H_{af} = 0$.

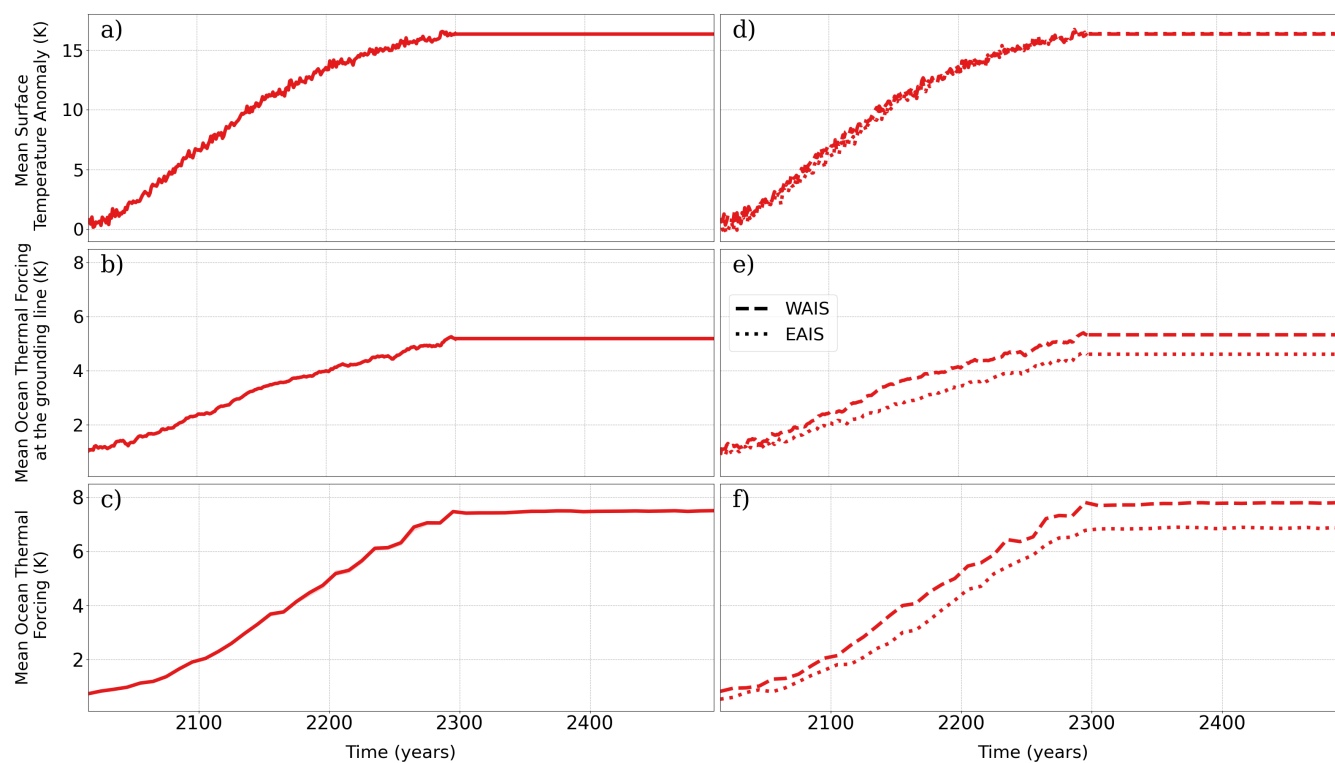


Figure A6. Mean evolution of the atmospheric (a), oceanic thermal forcing at the GL depth fixed in 2015 (b) and thermal forcing at the evolving GLs (c) in the AIS for CESM2-WACCM (SSP5-8.5) until year 2500. For (d), (e) and (f), same as in (a), (b) and (c), respectively, but for the WAIS and EAIS (modified from Juarez-Martinez et al., 2024).

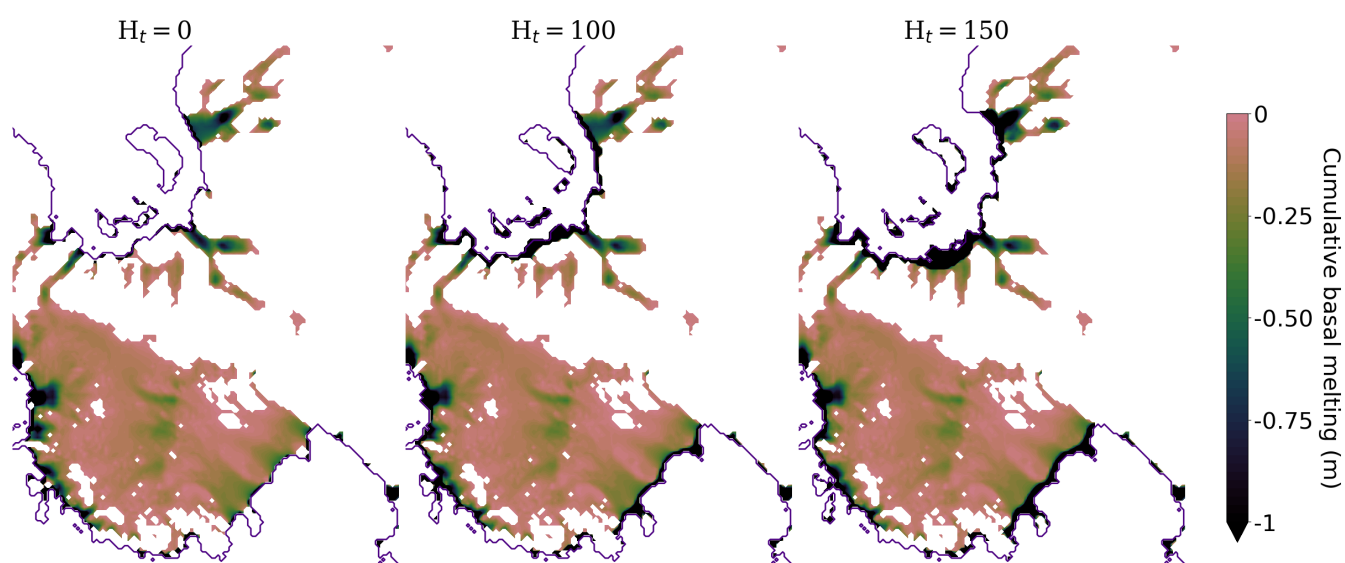


Figure A7. Zoom-in of cumulative basal mass balance w.r.t control at the initial time (m) until 2025 for different H_t values. GL as defined by $H_{af} = 0$ is shown in purple in order to better identify the area. Positive values have been masked.

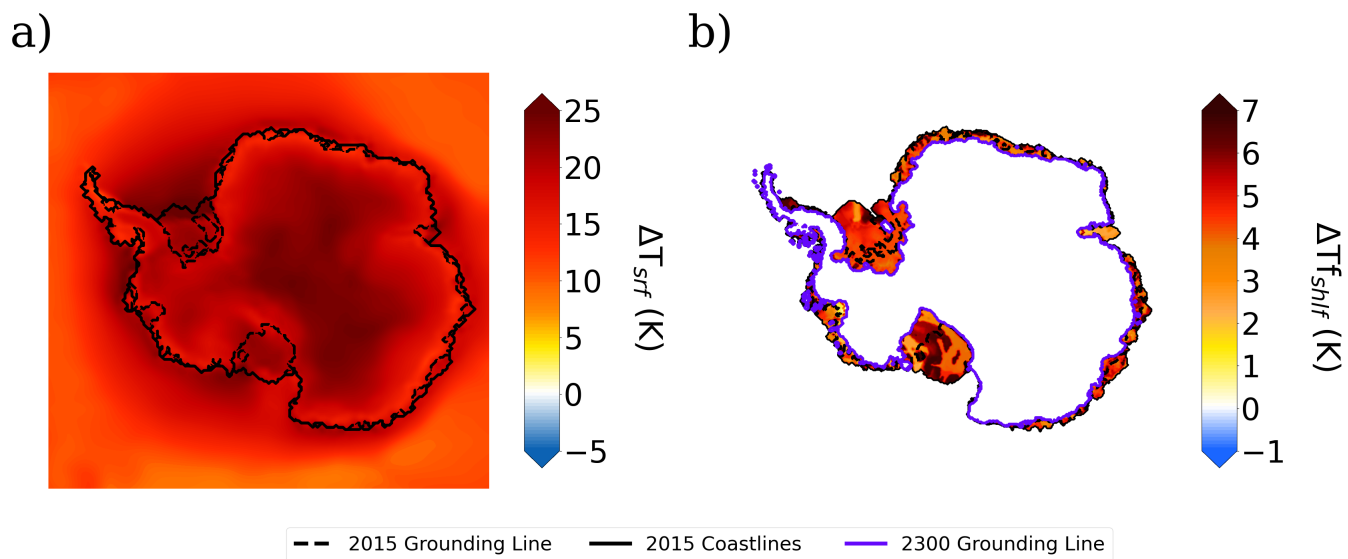


Figure A8. Anomalies in a) surface temperature (K) and b) thermal forcing (K) between 2300 and 2015 for CESM2-WACCM (SSP5-8.5) (modified from Juarez-Martinez et al., 2024).

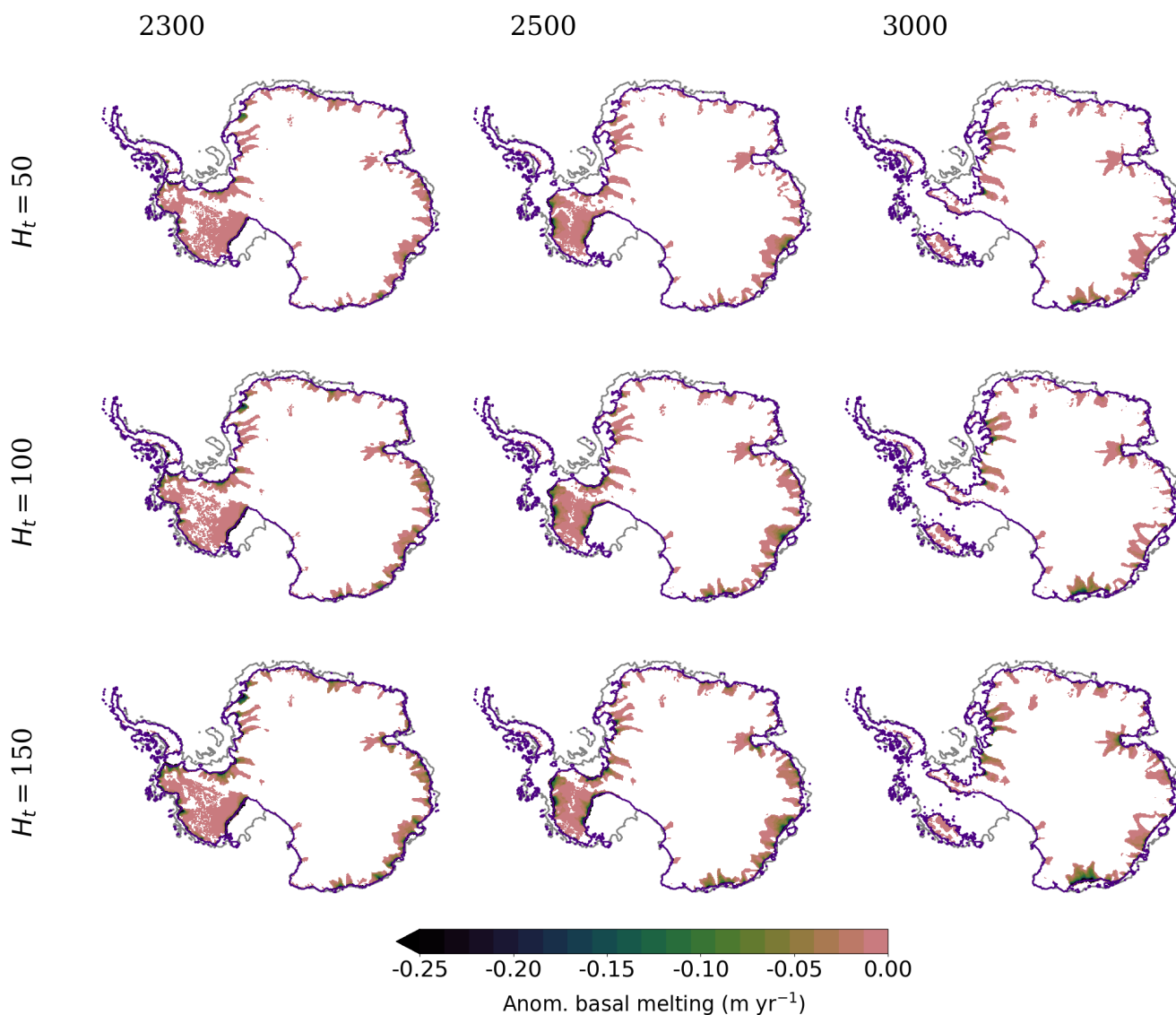


Figure A9. Basal melting anomalies (m yr⁻¹) for the different values of H_t at different timesteps with respect to the case where $H_t = 0$ m for the experiments with CESM2-WACCM (SSP5-8.5). The gray and purple lines represent the initial and evolving GL, respectively (defined as $H_{af} = 0$).



Table A1. Statistical values of the distribution of H_{af} (in m) for the observational datasets in Fig. 2: mean, median, standard deviation (σ), first quartile (Q1), third quartile (Q3), fifth percentile (p5) and 95th percentile (p95).

Dataset/Region	Mean	Median	σ	Q1	Q3	p5	p95
a) Thwaites Glacier	129.1	76.8	135.7	35.7	216.1	-9.7	406.0
b) Berry Glacier	35.8	37.1	47.0	3.7	71.3	-23.9	105.7
c) Rennick Glacier	17.0	14.0	35.9	-3.8	40.0	-38.1	73.5
d) Moscow University Glacier	43.6	38.1	48.1	11.7	75.0	-26.1	122.3
e) Totten Glacier	15.6	36.5	101.7	-20.4	73.4	-187.5	145.6
f) Amery Ice Shelf	36.9	18.1	155.3	-8.1	68.9	-193.7	375.7

Table A2. Summary of the SLC (m SLE) at 2100, 2300, 2500 and 3000 from the different AIS sectors at the two extreme values of H_t .

Year	AIS		WAIS		EAIS	
	$H_t = 0$	$H_t = 150$	$H_t = 0$	$H_t = 150$	$H_t = 0$	$H_t = 150$
2100	0.04	0.1	0.04	0.08	0	0.02
2300	2	2.5	1.3	1.5	0.7	1
2500	4.5	5.3	2.7	3	1.7	2.3
3000	7.6	9.2	4.5	4.6	3.1	4.6

Table A3. Percentage of increase (%) in SLC at 2100, 2300, 2500 and 3000 for the different values of H_t , relative to reference case $H_t = 0$.

Year	$H_t = 25$	$H_t = 50$	$H_t = 75$	$H_t = 100$	$H_t = 125$	$H_t = 150$
2100	22	46	73	98	120	177
2300	3	7	13	17	21	24
2500	3	6	10	14	18	19
3000	2	6	10	14	18	21



335 *Code availability.* The Yelmo ice sheet model is available at <https://github.com/palma-ice/yelmo> (Robinson et al., 2020). The FastIsostasy code is found at <https://github.com/palma-ice/FastIsostasy> (Swierczek-Jereczek et al., 2024). The coupled model is run within the YelmoX framework, found at <https://github.com/palma-ice/yelmox>. The versions used in the study can be found in the Zenodo repository 10.5281/zenodo.18762651 (Juarez-Martinez, 2025a).

Data availability. The output results from the simulations are available on the Zenodo repository 10.5281/zenodo.17098155 (Juarez-Martinez, 340 2025b).

Author contributions. AJM carried out the simulations. AR developed Yelmo and had the original idea for the parameterization. JSJ developed FastIsostasy and helped with the configuration of the simulations. All co-authors analyzed the results. AJM prepared the manuscript with contributions and revisions from all co-authors.

Competing interests. At least one of the (co-)authors is a member of the editorial board of The Cryosphere.

345 *Acknowledgements.* Antonio Juarez-Martinez acknowledges the funding received from the predoctoral grant partnership between the Complutense University of Madrid and Banco Santander (CT58/21- CT59/21), as well as the PalMA research group support during the creation of this manuscript. Jan Swierczek-Jereczek and Javier Blasco received funding from the EU H2020 research infrastructures of the European Commission (ClimTip, grant no. 101137601). Alexander Robinson received funding from the European Union (ERC, FORCLIMA; grant no. 101044247). This work also used resources of the Deutsches Klimarechenzentrum (DKRZ) granted by its Scientific Steering Committee 350 (WLA) under project ID ba1442.



References

- Alevropoulos-Borrill, A., Golledge, N. R., Cornford, S. L., Lowry, D. P., and Krapp, M.: Sustained ocean cooling insufficient to reverse sea level rise from Antarctica, *Communications Earth & Environment*, 5, 150, <https://doi.org/10.1038/s43247-024-01297-8>, 2024.
- Arthern, R. J. and Williams, C. R.: The sensitivity of West Antarctica to the submarine melting feedback, *Geophysical Research Letters*, 44, 2352–2359, <https://doi.org/10.1002/2017GL072514>, 2017.
- 355 Bett, D. T., Bradley, A. T., Williams, C. R., Holland, P. R., Arthern, R. J., and Goldberg, D. N.: Coupled ice–ocean interactions during future retreat of West Antarctic ice streams in the Amundsen Sea sector, *The Cryosphere*, 18, 2653–2675, <https://doi.org/10.5194/tc-18-2653-2024>, 2024.
- Blasco, J., Alvarez-Solas, J., Robinson, A., and Montoya, M.: Exploring the impact of atmospheric forcing and basal drag on the Antarctic Ice Sheet under Last Glacial Maximum conditions, *The Cryosphere*, 15, 215–231, <https://doi.org/10.5194/tc-15-215-2021>, 2021.
- 360 Bochow, N., Poltronieri, A., Robinson, A., Montoya, M., Rypdal, M., and Boers, N.: Overshooting the critical threshold for the Greenland ice sheet, *Nature*, 622, 528–536, <https://doi.org/10.1038/s41586-023-06503-9>, 2023.
- Bradley, A. T. and Hewitt, I. J.: Tipping point in ice-sheet grounding-zone melting due to ocean water intrusion, *Nature Geoscience*, 17, 631–637, <https://doi.org/10.1038/s41561-024-01465-7>, 2024.
- 365 Brancato, V., Rignot, E., Milillo, P., Morlighem, M., Mouginot, J., An, L., Scheuchl, B., Jeong, S., Rizzoli, P., Bueso Bello, J. L., and Prats-Iraola, P.: Grounding Line Retreat of Denman Glacier, East Antarctica, Measured With COSMO-SkyMed Radar Interferometry Data, *Geophysical Research Letters*, 47, e2019GL086291, <https://doi.org/10.1029/2019GL086291>, 2020.
- Bueler, E. and van Pelt, W.: Mass-conserving subglacial hydrology in the Parallel Ice Sheet Model version 0.6, *Geoscientific Model Development*, 8, 1613–1635, <https://doi.org/10.5194/gmdd-7-4705-2014>, 2015.
- 370 Chen, H., Rignot, E., Scheuchl, B., and Ehrenfeucht, S.: Grounding zone of Amery ice shelf, Antarctica, from differential synthetic-aperture radar interferometry, *Geophysical Research Letters*, 50, e2022GL102430, <https://doi.org/10.1029/2022GL102430>, 2023.
- Chen, H., Rignot, E., Scheuchl, B., Milillo, P., Morlighem, M., Gadi, R., Ciraci, E., Kim, J. H., and Dini, L.: Rapid retreat of Berry Glacier, West Antarctica, linked to seawater intrusions revealed by radar interferometry, *Nature Communications*, 16, 9292, <https://doi.org/10.1038/s41467-025-64330-0>, 2025.
- 375 Ciraci, E., Rignot, E., Scheuchl, B., Tolpekin, V., Wollersheim, M., An, L., Milillo, P., Bueso-Bello, J.-L., Rizzoli, P., and Dini, L.: Melt rates in the kilometer-size grounding zone of Petermann Glacier, Greenland, before and during a retreat, *Proceedings of the National Academy of Sciences*, 120, e2220924 120, <https://doi.org/10.1073/pnas.2220924120>, 2023.
- Coulon, V., Klose, A. K., Kittel, C., Edwards, T., Turner, F., Winkelmann, R., and Pattyn, F.: Disentangling the drivers of future Antarctic ice loss with a historically calibrated ice-sheet model, *The Cryosphere*, 18, 653–681, <https://doi.org/10.5194/tc-18-653-2024>, 2024.
- 380 Coulon, V., Klose, A. K., Edwards, T., Turner, F., Pattyn, F., and Winkelmann, R.: From short-term uncertainties to long-term certainties in the future evolution of the Antarctic Ice Sheet, *Nature communications*, 16, 10385, <https://doi.org/10.1038/s41467-025-66178-w>, 2025.
- Dee, D. P., Uppala, S. M., Simmons, A. J., Berrisford, P., Poli, P., Kobayashi, S., Andrae, U., Balmaseda, M., Balsamo, G., Bauer, d. P., et al.: The ERA-Interim reanalysis: Configuration and performance of the data assimilation system, *Quarterly Journal of the royal meteorological society*, 137, 553–597, <https://doi.org/10.1002/qj.828>, 2011.
- 385 Diener, T., Sasgen, I., Agosta, C., Fürst, J. J., Braun, M. H., Konrad, H., and Fettweis, X.: Acceleration of dynamic ice loss in Antarctica from satellite gravimetry, *Frontiers in Earth Science*, 9, 741789, <https://doi.org/10.3389/feart.2021.741789>, 2021.



- Fox-Kemper, B., Hewitt, H., Xiao, C., Aasgeirsdottir, G., and et al.: Ocean, cryosphere and sea level change, p. 1211–1361, Chapter 9, Cambridge University Press, https://www.ipcc.ch/report/ar6/wg1/downloads/report/IPCC_AR6_WGI_Chapter09.pdf, 2021.
- Freer, B. I., Marsh, O. J., Hogg, A. E., Fricker, H. A., and Padman, L.: Modes of Antarctic tidal grounding line migration revealed by ICESat-2 laser altimetry, *The Cryosphere Discussions*, 2023, 1–35, <https://doi.org/10.5194/tc-2022-265>, 2023.
- 390 Fricker, H. A., Galton-Fenzi, B. K., Walker, C. C., Freer, B. I. D., Padman, L., and DeConto, R.: Antarctica in 2025: Drivers of deep uncertainty in projected ice loss, *Science*, 387, 601–609, <https://doi.org/10.1126/science.adt9619>, 2025.
- Gadi, R., Rignot, E., and Menemenlis, D.: Modeling ice melt rates from seawater intrusions in the grounding zone of Petermann Gletscher, Greenland, *Geophysical Research Letters*, 50, <https://doi.org/10.1029/2023GL105869>, 2023.
- 395 Goelzer, H., Coulon, V., Pattyn, F., de Boer, B., and van de Wal, R.: Brief communication: On calculating the sea-level contribution in marine ice-sheet models, *The Cryosphere*, 14, 833–840, <https://doi.org/10.5194/tc-14-833-2020>, 2020.
- Greene, C. A., Gardner, A. S., Schlegel, N.-J., and Fraser, A. D.: Antarctic calving loss rivals ice-shelf thinning, *Nature*, 609, 948–953, <https://doi.org/10.1038/s41586-022-05037-w>, 2022.
- Greve, R. and Blatter, H.: *Dynamics of ice sheets and glaciers*, Springer Science & Business Media, 2009.
- 400 Gutiérrez-González, L., Robinson, A., Alvarez-Solas, J., Tabone, I., Swierczek-Jereczek, J., Moreno-Parada, D., and Montoya, M.: Hysteresis of the Greenland ice sheet from the Last Glacial Maximum to the future, *EGUsphere*, <https://doi.org/10.5194/egusphere-2025-2616>, preprint, 2025.
- Hanna, E., Topál, D., Box, J. E., Buzzard, S., Christie, F. D. W., Hvidberg, C., Morlighem, M., De Santis, L., Silvano, A., Colleoni, F., Sasgen, I., Banwell, A. F., van den Broeke, M. R., DeConto, R., De Rydt, J., Goelzer, H., Gossart, A., Gudmundsson, G. H., Lindbäck, K., Miles, B., Mottram, R., Pattyn, F., Reese, R., Rignot, E., Srivastava, A., Sun, S., Toller, J., Tuckett, P. A., and Ultee, L.: Short- and long-term variability of the Antarctic and Greenland ice sheets, *Nature Reviews Earth & Environment*, 5, 193–210, <https://doi.org/10.1038/s43017-023-00509-7>, 2024.
- 405 Hill, E., Gudmundsson, G., and Chandler, D.: Ocean warming as a trigger for irreversible retreat of the Antarctic ice sheet, *Nature Climate Change*, 14, 1165–1171, <https://doi.org/10.1038/s41558-024-02134-8>, 2024.
- 410 Horgan, H., Alley, R., Christianson, K., Jacobel, R., Anandakrishnan, S., Muto, A., Beem, L., and Siegfried, M.: Estuaries beneath ice sheets, *Geology*, 41, textit[in press], <https://doi.org/10.1130/G34654.1>, 2013.
- Joughin, I., Smith, B., and Schoof, C.: Regularized Coulomb Friction Laws for Ice Sheet Sliding: Application to Pine Island Glacier, Antarctica, *Geophysical Research Letters*, 46, <https://doi.org/10.1029/2019GL082526>, 2019.
- Jourdain, N. C., Asay-Davis, X., Hattermann, T., Straneo, F., Seroussi, H., Little, C. M., and Nowicki, S.: A protocol for calculating basal melt rates in the ISMIP6 Antarctic ice sheet projections, *The Cryosphere*, 14, 3111–3134, <https://doi.org/10.5194/tc-14-3111-2020>, 2020.
- 415 Juarez-Martinez, A.: Code versions for the article: "Parameterizing tidal-water intrusions in long-term Antarctic ice-sheet projections", <https://doi.org/10.5281/zenodo.18762651>, code versions, 2025a.
- Juarez-Martinez, A.: Output results from the article (preprint): "Parameterizing tidal-water intrusions in long-term Antarctic ice-sheet projections", <https://doi.org/10.5281/zenodo.17098155>, preprint data set, 2025b.
- 420 Juarez-Martinez, A., Blasco Navarro, J., Robinson, A., Montoya, M., and Alvarez-Solas, J.: Antarctic sensitivity to oceanic melting parameterizations, *The Cryosphere*, 18, 4257–4283, <https://doi.org/10.5194/tc-18-4257-2024>, 2024.
- Kim, J., Rignot, E., Holland, D., and Holland, D.: Seawater Intrusion at the Grounding Line of Jakobshavn Isbræ, Greenland, From Terrestrial Radar Interferometry, *Geophysical Research Letters*, 51, <https://doi.org/10.1029/2023GL106181>, 2024.



- Leguy, G., Lipscomb, W., and Asay-Davis, X.: Marine ice sheet experiments with the Community Ice Sheet Model, *The Cryosphere*, 15, 425 3229–3253, <https://doi.org/10.5194/tc-15-3229-2021>, 2021.
- Lipscomb, W., Leguy, G., Jourdain, N., Asay-Davis, X., Seroussi, H., and Nowicki, S.: ISMIP6-based projections of ocean-forced Antarctic Ice Sheet evolution using the Community Ice Sheet Model, *The Cryosphere*, 15, 633–661, <https://doi.org/10.5194/tc-15-633-2021>, 2021.
- Lipscomb, W. H., Price, S. F., Hoffman, M. J., Leguy, G. R., Bennett, A. R., Bradley, S. L., Evans, K. J., Fyke, J. G., Kennedy, J. H., Perego, M., Ranken, D. M., Sacks, W. J., Salinger, A. G., Vargo, L. J., and Worley, P. H.: Description and evaluation of the Community Ice Sheet Model (CISM) v2.1, *Geoscientific Model Development*, 12, 387–424, <https://doi.org/10.5194/gmd-12-387-2019>, 2019.
- Lloyd, A. J., Crawford, O., Al-Attar, D., Austermann, J., Hoggard, M. J., Richards, F. D., and Syvret, F.: GIA imaging of 3-D mantle viscosity based on palaeo sea level observations – Part I: Sensitivity kernels for an Earth with laterally varying viscosity, *Geophysical Journal International*, 236, 1139–1171, <https://doi.org/10.1093/gji/ggad455>, 2024.
- MacGregor, J., Anandakrishnan, S., Catania, G., and Winebrenner, D.: The grounding zone of the Ross Ice Shelf, West Antarctica, from ice-penetrating radar, *Journal of Glaciology*, 57, 917–928, <https://doi.org/10.3189/002214311798043780>, 2011.
- Marsh, O., Arthern, R., and Rydt, J.: Ocean tides trigger ice shelf rift growth and calving, *Nature Communications*, 16, <https://doi.org/10.1038/s41467-025-61796-w>, 2025.
- Miles, B. and Bingham, R.: Progressive unanchoring of Antarctic ice shelves since 1973, *Nature*, 626, 785–791, <https://doi.org/10.1038/s41586-024-07049-0>, 2024.
- Milillo, P., Rignot, E., Mouginot, J., Scheuchl, B., Morlighem, M., Li, X., and Salzer, J. T.: On the Short-term Grounding Zone Dynamics of Pine Island Glacier, West Antarctica, Observed With COSMO-SkyMed Interferometric Data, *Geophysical Research Letters*, 44, 10,436–10,444, <https://doi.org/10.1002/2017GL074320>, 2017.
- Milillo, P., Rignot, E., Rizzoli, P., Scheuchl, B., Mouginot, J., Bueso, J., and Prats-Iraola, P.: Heterogeneous retreat and ice melt of Thwaites Glacier, West Antarctica, *Science Advances*, 5, <https://doi.org/10.1126/sciadv.aau3433>, 2019.
- Milillo, P., Rignot, E., Rizzoli, P., Scheuchl, B., Mouginot, J., Bueso, J., Prats-Iraola, P., and Dini, L.: Rapid glacier retreat rates observed in West Antarctica, *Nature Geoscience*, 15, <https://doi.org/10.1038/s41561-021-00877-z>, 2022.
- Mohajerani, Y., Jeong, S., Scheuchl, B., Velicogna, I., Rignot, E., and Milillo, P.: Automatic delineation of glacier grounding lines in differential interferometric synthetic-aperture radar data using deep learning, *Scientific Reports*, 11, <https://doi.org/10.1038/s41598-021-84309-3>, 2021.
- Moreno-Parada, D., Alvarez-Solas, J., Blasco Navarro, J., Montoya, M., and Robinson, A.: Simulating the Laurentide Ice Sheet of the Last Glacial Maximum, *The Cryosphere*, 17, 2139–2156, <https://doi.org/10.5194/tc-17-2139-2023>, 2023.
- Morlighem, M., Rignot, E., Binder, T., Blankenship, D., Drews, R., Eagles, G., Eisen, O., Ferraccioli, F., Forsberg, R., Fretwell, P., Goel, V., Greenbaum, J., Gudmundsson, G., Guo, J., Helm, V., Hofstede, C., Howat, I., Humbert, A., Jokat, W., and Young, D.: Deep glacial troughs and stabilizing ridges unveiled beneath the margins of the Antarctic ice sheet, *Nature Geoscience*, 13, 1–6, <https://doi.org/10.1038/s41561-019-0510-8>, 2020.
- Morlighem, M. et al.: IceBridge BedMachine Greenland, Version 5, <https://doi.org/10.5067/GMEVBWFLWA7X>, 2022.
- Otosaka, I., Horwath, M., Mottram, R., and Nowicki, S.: Mass Balances of the Antarctic and Greenland Ice Sheets Monitored from Space, *Surveys in Geophysics*, 44, 1–38, <https://doi.org/10.1007/s10712-023-09795-8>, 2023.
- Paolo, F., Gardner, A., Greene, C., Nilsson, J., Schodlok, M. P., Schlegel, N.-J., and Fricker, H.: Widespread slowdown in thinning rates of West Antarctic ice shelves, *The Cryosphere*, 17, 3409–3433, <https://doi.org/10.5194/tc-17-3409-2023>, 2023.



- Parizek, B.: Grounding Zones: The “Inland” Dynamic Interface Between Seawater, Outlet Glaciers, Subglacial Meltwater Routing, and Ice-Shelf Processes, *Geophysical Research Letters*, 51, <https://doi.org/10.1029/2024GL110427>, 2024.
- Pattyn, F.: The paradigm shift in Antarctic ice sheet modelling, *Nature Communications*, 9, <https://doi.org/10.1038/s41467-018-05003-z>, 2018.
- 465 Pritchard, H., Fretwell, P., Fremant, A., Bodart, J., Kirkham, J., Aitken, A., Bamber, J., Bell, R., Bianchi, C., Bingham, R. G., Blankenship, D., Casassa, G., Christianson, K., Conway, H., Corr, H., Xiangbin, C., Damaske, D., Damm, V., Dorschel, B., and Zirizzotti, A.: Bedmap3 updated ice bed, surface and thickness gridded datasets for Antarctica, *Scientific Data*, 12, <https://doi.org/10.1038/s41597-025-04672-y>, 2025.
- Reese, R., Albrecht, T., Mengel, M., and Asay-Davis, X.: Antarctic sub-shelf melt rates via PICO, *The Cryosphere*, 12, 1969–1985, <https://doi.org/10.5194/tc-12-1969-2018>, 2018.
- 470 Rignot, E., Mouginot, J., and Scheuchl, B.: Antarctic Grounding Line Mapping from Differential Satellite Radar Interferometry, *Geophys. Res. Lett.*, 38, <https://doi.org/10.1029/2011GL047109>, 2011.
- Rignot, E., Ciraci, E., Scheuchl, B., Tolpekin, V., Wollersheim, M., and Dow, C.: Widespread seawater intrusions beneath the grounded ice of Thwaites Glacier, West Antarctica, *Proceedings of the National Academy of Sciences*, 121, e2404766 121, <https://doi.org/10.1073/pnas.2404766121>, 2024.
- 475 Robel, A. A., Wilson, E., and Seroussi, H.: Layered seawater intrusion and melt under grounded Ice, *The Cryosphere*, 16, 451–469, <https://doi.org/10.5194/tc-16-451-2022>, 2022.
- Robinson, A., Alvarez-Solas, J., Montoya, M., Goelzer, H., Greve, R., and Ritz, C.: Description and validation of the ice-sheet model Yelmo (version 1.0), *Geoscientific Model Development*, 13, 2805–2823, <https://doi.org/10.5194/gmd-13-2805-2020>, 2020.
- 480 Robinson, A., Goldberg, D., and Lipscomb, W. H.: A comparison of the stability and performance of depth-integrated ice-dynamics solvers, *The Cryosphere*, 16, 689–709, <https://doi.org/10.5194/tc-16-689-2022>, 2022.
- Rosier, S. H. and Gudmundsson, G. H.: Exploring mechanisms responsible for tidal modulation in flow of the Filchner–Ronne Ice Shelf, *The Cryosphere*, 14, 17–37, <https://doi.org/10.5194/tc-14-17-2020>, 2020.
- Ross, N., Milillo, P., Nakshatrala, K., Ballarini, R., Stubblefield, A., and Dini, L.: Importance of ice elasticity in simulating tide-induced grounding line variations along prograde bed slopes, *The Cryosphere*, 19, 1995–2015, <https://doi.org/10.5194/tc-19-1995-2025>, 2025.
- 485 Schoof, C.: Ice Sheet Grounding Line Dynamics: Steady States, Stability, and Hysteresis, *Journal of Geophysical Research*, 112, F03S28, <https://doi.org/10.1029/2006JF000664>, 2007.
- Seroussi, H. and Morlighem, M.: Representation of basal melting at the grounding line in ice flow models, *The Cryosphere*, 12, 3085–3096, <https://doi.org/10.5194/tc-12-3085-2018>, 2018.
- 490 Seroussi, H., Nowicki, S., Payne, A., Goelzer, H., Lipscomb, W., Abe-Ouchi, A., Agosta, C., Albrecht, T., Asay-Davis, X., Barthel, A., Calov, R., Cullather, R., Dumas, C., Galton-Fenzi, B. K., Gladstone, R., Golledge, N., Gregory, J. M., Greve, R., Hattermann, T., and Zwinger, T.: ISMIP6 Antarctica: a multi-model ensemble of the Antarctic ice sheet evolution over the 21st century, *The Cryosphere*, 14, 3033–3070, <https://doi.org/10.5194/tc-14-3033-2020>, 2020.
- Seroussi, H., Pelle, T., Lipscomb, W., Abe-Ouchi, A., Albrecht, T., Alvarez-Solas, J., Asay-Davis, X., Barré, J. B., Berends, C., Bernales, J., Blasco Navarro, J., Caillet, J., Chandler, D., Coulon, V., Cullather, R., Dumas, C., Galton-Fenzi, B., Garbe, J., Gillet-Chaulet, F., and Zwinger, T.: Evolution of the Antarctic Ice Sheet Over the Next Three Centuries From an ISMIP6 Model Ensemble, *Earth’s Future*, 12, <https://doi.org/10.1029/2024EF004561>, 2024.



- Shepherd, A., Gilbert, L., Muir, A., Konrad, H., McMillan, M., Slater, T., Briggs, K., Sundal, A., Hogg, A., and Engdahl, M.: Trends in Antarctic Ice Sheet Elevation and Mass, *Geophysical Research Letters*, 46, 8174–8183, <https://doi.org/10.1029/2019GL082182>, 2019.
- 500 Swierczek-Jereczek, J., Montoya, M., Latychev, K., Robinson, A., Alvarez-Solas, J., and Mitrovica, J.: FastIsostasy v1.0 – a regional, accelerated 2D glacial isostatic adjustment (GIA) model accounting for the lateral variability of the solid Earth, *Geoscientific Model Development*, 17, 5263–5290, <https://doi.org/10.5194/gmd-17-5263-2024>, 2024.
- Tsai, V. and Gudmundsson, G.: An improved model for tidally modulated grounding-line migration, *Journal of Glaciology*, 61, 216–222, <https://doi.org/10.3189/2015JoG14J152>, 2015.
- 505 Turney, C. S. M., Fogwill, C. J., Golleddge, N. R., McKay, N. P., van Sebille, E., Jones, R. T., Etheridge, D., Rubino, M., Thornton, D. P., Davies, S. M., Ramsey, C. B., Thomas, Z. A., Bird, M. I., Munksgaard, N. C., Kohno, M., Woodward, J., Winter, K., Weyrich, L. S., Rootes, C. M., Millman, H., Albert, P. G., Rivera, A., van Ommen, T., Curran, M., Moy, A., Rahmstorf, S., Kawamura, K., Hillenbrand, C.-D., Weber, M. E., Manning, C. J., Young, J., and Cooper, A.: Early Last Interglacial ocean warming drove substantial ice mass loss from Antarctica, *Proceedings of the National Academy of Sciences*, 117, 3996–4006, <https://doi.org/10.1073/pnas.1902469117>, 2020.
- 510 Van Wessem, J. M., Reijmer, C., Morlighem, M., Mouginit, J., Rignot, E., Medley, B., Joughin, I., Wouters, B., Depoorter, M., Bamber, J., Lenaerts, J., Berg, W., Van den Broeke, M., and Meijgaard, E.: Improved representation of East Antarctic surface mass balance in a regional atmospheric climate model, *Journal of Glaciology*, 60, 761–770, <https://doi.org/10.3189/2014JoG14J051>, 2014.
- Weertman, J.: Stability of the Junction of an Ice Sheet and an Ice Shelf, *Journal of Glaciology*, 13, 3–11, <https://doi.org/10.3189/S0022143000023327>, 1974.
- 515 Williams, C. R., Thodoroff, P., Arthern, R., Byrne, J., Hosking, S., Kaiser, M., Lawrence, N., and Kazlauskaitė, I.: Calculations of extreme sea level rise scenarios are strongly dependent on ice sheet model resolution, *Communications Earth & Environment*, 6, <https://doi.org/10.1038/s43247-025-02010-z>, 2025.
- Wilson, E., Wells, A., Hewitt, I., and Cenedese, C.: The dynamics of a subglacial salt wedge, *Journal of Fluid Mechanics*, 895, <https://doi.org/10.1017/jfm.2020.308>, 2020.
- 520 Winkelmann, R., Martin, M., Haseloff, M., Albrecht, T., Bueler, E., Khroulev, C., and Levermann, A.: The potsdam parallel ice sheet model (PISM-PIK) – Part 1: Model description, *The Cryosphere*, 5, 715–726, <https://doi.org/10.5194/tc-5-715-2011>, 2011.
- Zhu, Y., Hogg, A. E., Hooper, A., and Wallis, B. J.: Short and Long-term Grounding Zone Dynamics of Amery Ice Shelf, East Antarctica, *The Cryosphere*, 19, 3971–3989, <https://doi.org/10.5194/tc-19-3971-2025>, 2025.
- Zoet, L. K. and Iverson, N. R.: A slip law for glaciers on deformable beds, *Science*, 368, 76–78, <https://doi.org/10.1126/science.aaz1183>,
525 2020.